INVESTIGATION OF A POLARIZATION CONTROLLER IN TITANIUM DIFFUSED LITHIUM NIOBATE WAVEGUIDE NEAR 1530 NM WAVELENGTH

A Dissertation

by

WON JU SUNG

Submitted to the Office of Graduate and Professional Studies of
Texas A&M University
in partial fulfillment of the requirements for the degree of

DOCTOR OF PHILOSOPHY

Chair of Committee,	Ohannes Eknoyan
Committee Members,	Christi K. Madsen
	Alvin T. Yeh
	Byung-Jun Yoon
Head of Department,	Chanan Singh

December 2013

Major Subject: Electrical Engineering

ABSTRACT

Optical polarization control in Ti diffused channel waveguides onto $LiNbO_3$ substrates have been investigated near 1530 nm wavelength regime by utilizing electro-optic effects of the substrate material. A device configuration composed of two polarization converters with a phase shifter centered between them and all integrated on a single optical channel waveguide was used. The polarization converters provided a means to control the polarization, and the phase shifter offered a tool to maintain the required phase condition between them. Single mode channel waveguides were fabricated by diffusing 7μm-wide Ti stripes into the $LiNbO_3$ substrate. The polarization converters and phase shifter were formed by patterning aluminum surface electrodes on top of a SiO_2 buffer layer. The polarization converters were produced in an interdigitated electrode form with a spatial period of 21 μm, over 10.5 mm coupling length. The phase shifter was implemented in the form of a 6,000 μm long electrode with 17 μm gap. The characteristics of each electro-optic element in the integrated configuration were individually evaluated first, and then the behavior of the overall device as a polarization controller was investigated. Polarization conversion efficiency of 99.5% between TE and TM orthogonal modes was realized for the converters, and π-radian phase shift between orthogonal modes was achieved with 40 V on the phase shifter. Using an optical vector analyzer (OVA) for characterizing the output, transformation of orthogonal or arbitrary incident polarization to either TE or TM polarization at the output was successfully realized. Suppression for the unwanted

polarization at the output of approximately -40 dB near 1529.4 nm wavelength was obtained with voltages on both converters for TE↔TM transformation, as well as 45^{o} and 56^{o} incident polarization. For the incident orthogonal polarization case the transformation was realized without a voltage on the phase shifter supporting the implemented design parameters, and transformation of the obtained output back to its incident polarization through an induced π-radian retardation was confirmed by applying 40 V on the phase shifter.

DEDICATION

To my family

ACKNOWLEDGEMENTS

I would like to thank my advisor and committee chair, Dr. Ohannes Eknoyan, for his advice and concerns over the last five years. Also, I would like to express my appreciation to my committee members, Dr. Christi K. Madsen, Dr. Alvin T. Yeh, and Dr. Byung-Jun Yoon for their time and guidance throughout the this research.

I appreciate to Mr. Robert Atkins, Mr. Jim Gardner, and Mr. Denny Spears for their technical support and help throughout every step of this research. They have been great staffs with full of experiences and technical knowledge. There are many friends and colleagues such as Yong-Wook, Jaehyun, Jaewoo, Chiwan, Jaewon, Hyunsoo, Tim and Travis. I would like to thank them for a lot of memories that I can share with them.

Finally, I'd like to thank to my wife for her patience and love and my family in Korea for their encouragement.

TABLE OF CONTENTS

LIST OF FIGURES

LIST OF TABLES

TABLE Page

CHAPTER I

INTRODUCTION

Ever since the internet was developed, the amount of data transfer has been growing enormously. Now the internet has become not an option but one of the necessities in our life. Furthermore, the development of new technologies like Voice over internet protocol communication including video requires more data transfer. Moreover, high capacity data services such as Video-On-Demand and online broadcasting services increased data usage explosively. As such, the development of data transfer technologies has been ensuing to catch up those new data services' needs, and fiber optic communication has been especially in the middle of it.

In addition, recent research reveals that high speed optical signal processing is an important issue as well. Optical signal has been replacing electric signal in data transmission and several optical components have been developed to support high speed data transfer. Already 40G/100G optical communication systems are being commercialized [1-3], and efforts for 400G modulators are being pursued [1, 4]. Various materials have been explored for high speed devices need [5, 6], and lithium niobate remains the most attractive choice currently [7].

Fiber optic communication is a key technology to enable high capacity data transfer in high capacity data transfer systems. Among several technologies in fiber optic communication, dense wavelength division multiplexing (DWDM) is emerging as a

dominant technique. DWDM technique divides a transmitted light spectrum into multiple channels, and provides a venue for exploiting the optical bandwidth [8, 9].

As numerous types of optical components have been developed and optical signals have been gradually replacing electrical signals, the integration of optical components has become essential. One of the important issues in optical integration is polarization. Most optical components are polarization dependent, and the preservation of polarization of an optical signal is essential for the efficient operation of integrated optical chips. In previous research at Texas A&M [10], the integration of chalcogenide ring resonator and Ti diffused waveguide was demonstrated. However, it was functional only with TM polarization, thus the necessity of polarization control emerged as an area of interest for investigation.

In this research, the device has also been evaluated as a polarization controller, and is capable of providing 'dynamic control' for transforming any input state of polarization (SOP) into any desired output SOP. Researches on polarization control have been active for the past few decades. Since long-haul communication links was employed, polarization mode dispersion (PMD) or polarization dependent loss (PDL) have been issues [11]. Also, for realizing high speed communication, efforts for an implementation of polarization related techniques such as phase shift keying (PSK) and coherent detection have been pursued, and so polarization control has been obtaining attention again [12]. Researches have been utilized several materials and various schemes. Table 1 summarizes researches on polarization control.

Table 1 Summary of Researches on Polarization Control

Arthur	Year	Structure	Material
H. Shimizu K. Kaede [13]	1988	QWP-HWP	$LiNbO_3$
R. Noeet al. [14]	1988	3 or 4 retarders	Fiber squeezers
F. Heismann [15, 16]	1989, 1990	Multiple sets of a retarder and a coupler	$LiNbO_3$
L. Moller [17]	2001	2 Couplers and one retarder	Algorithm
M. Martinelli R.A. Chipman [18]	2003	2 retarders	Liquid cells
P.Oswald C.K. Madsen [19]	2006	PS-DC-PS DC-PS-DC	Algorithm
B.Koch et al. [20]	2012	SBC integration	$LiNbO_3$

Noe proposed the scheme for polarization control with two couplers and one retarder employing fiber squeezers [14]. In this work, the scheme is demonstrated by utilizing $LiNbO_3$ and the electro-optic effect.

Chapter II provides a brief theoretical review of optical wave propagation, electro-optic effect, and polarization control. Analyses of the device structure are given in Chapter III. Device fabrication is presented in Chapter IV, and is followed by a discussion of the experimental results in Chapter V. Finally, concluding remarks are made in Chapter VI.

CHAPTER II

THEORETICAL REVIEW

In this chapter, optical plane wave propagation in dielectric media are reviewed based on Maxwell's equations. An overview of optical wave propagation in optical dielectric waveguides is presented. The electro-optic effect is introduced and polarization conversion is outlined. The operating principles of polarization controller are explained.

A. Basic Theory of Wave Propagation

An optical wave is composed of coupled electric and magnetic fields, which in a lossless dielectric medium and away from sources can be obtained from solutions of Maxwell's equations,[21]

$$\nabla \times \mathbf{E} = -\frac{\partial \mathbf{B}}{\partial t} \tag{1}$$

$$\nabla \times \mathbf{H} = \frac{\partial \mathbf{D}}{\partial t} \tag{2}$$

$$\nabla \cdot \mathbf{D} = 0 \tag{3}$$

$$\nabla \cdot \mathbf{B} = 0. \tag{4}$$

Where **E** represents the electric field intensity vector (V/m), **H** is the magnetic field intensity vector (A/m), and **D** (C/m^2) and **B** (Wb/m^2) are the electric and magnetic displacement vectors, respectively. The dielectric permittivity ε (F/m) of the medium

defines the relation between **E** and **D**, and the permeability of free space μ_o (H/m) relates **H** to **B**. In a homogeneous, isotropic medium the relationships are

$$\mathbf{D} = \varepsilon\mathbf{E} + \mathbf{P} = \varepsilon\mathbf{E} \tag{5}$$

$$\mathbf{B} = \mu_o\mathbf{H} \tag{6}$$

with $\varepsilon = \varepsilon_o \cdot \varepsilon_r = \varepsilon_o \cdot n^2$ at optical frequencies, and n is the refractive index of the material.

Taking the curl of equation (1), and using a relevant vector identity along with equations (2), (5) and (6), leads to the well-known wave equation

$$\nabla^2\mathbf{E} - \varepsilon\mu_o \frac{\partial^2\mathbf{E}}{\partial t^2} = 0\,. \tag{7}$$

For a monochromatic wave of angular frequency $\omega = \frac{2\pi c}{\lambda}$, the electric field vector **E** can be written as:

$$\mathbf{E}(r,t) = \mathbf{E}(r)e^{j\omega t}\,. \tag{8}$$

Substituting equation (8) into equation (7) yields

$$\nabla^2\mathbf{E}(r) + n^2k_o^2\mathbf{E}(r) = 0 \tag{9}$$

where $k_o = \frac{\omega}{c}$ is the propagation constant in free space , $c = \frac{1}{\sqrt{\mu_o\varepsilon_o}}$ is the speed of light in free space, and $n = \sqrt{\varepsilon_r}$ is the refractive index of the medium.

B. Optical Waveguides

The planar asymmetric dielectric waveguide shown in figure 1 is the simplest configuration for describing propagation in optical waveguides. It consists of a high refractive index region (n_g) surrounded by low refractive index media (n_c, n_s). The high index center region, which is the guiding layer, provides a pathway for the energy confinement of optical waves.

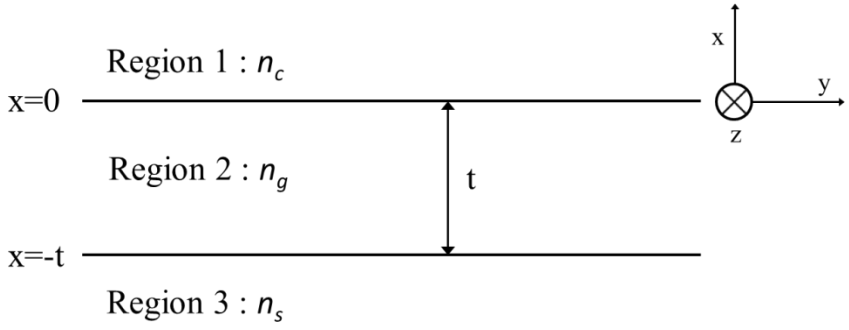

Fig. 1. Asymmetric planar dielectric waveguide.

Assuming forward propagation in the y direction, and semi-infinite planes at the interfaces (i.e.; z=∞, hence $\partial/\partial z = \partial^2/\partial z^2 = 0$), equation (9) can be written for each region separately as,

$$\frac{d^2}{dx^2}\mathbf{E}(x) + \left(k_o^2 n_c^2 - \beta^2\right)\mathbf{E}(x) = 0 \qquad 0 < x \tag{11}$$

$$\frac{d^2}{dx^2}\mathbf{E}(x) + \left(k_o^2 n_g^2 - \beta^2\right)\mathbf{E}(x) = 0 \qquad -t < x < 0 \tag{12}$$

$$\frac{d^2}{dx^2}\mathbf{E}(x) + \left(k_o^2 n_s^2 - \beta^2\right)\mathbf{E}(x) = 0 . \qquad \text{x < -t} \tag{13}$$

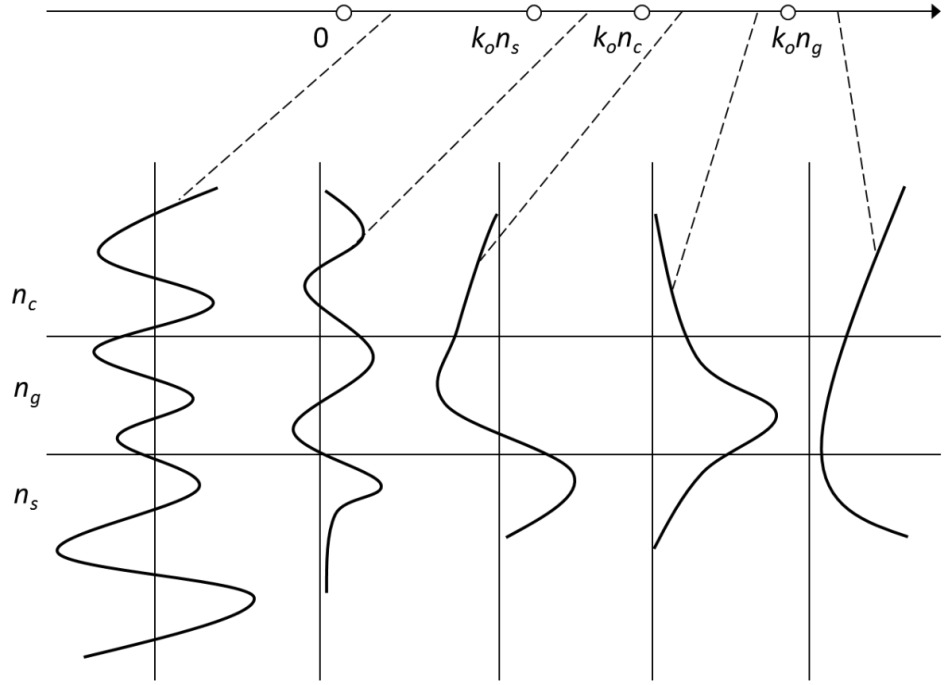

Fig. 2. The electric field distributions of the three-layer planar waveguide based on the value of propagation constant (β).

Only if $k_o^2 n_i^2 - \beta^2$, where i = g, c or s, is positive, oscillatory solutions along the x-axis would be possible in each region. Energy confinement, however, requires that the distribution of the electric for a propagating wave can have an oscillatory solution along the x-axis in the high index center region but must decay exponentially in the surrounding outer regions. Thus, the distribution of the electric field along the x-axis

would depend on the value of β. For the shown refractive indices of regions in figure 1, $n_g > n_s > n_c$, the field distributions corresponding to different values of β are depicted in figure 2. Guided wave propagation would only be possible for $k_o n_s < \beta < k_o n_g$.

A planar waveguide supports a finite number of optical modes along the energy confinement direction of a guided-wave depending on the structure of the waveguide. Optical modes can be grouped into orthogonal TE and TM polarization modes based on existing field components of the propagating wave. For transverse electric (TE) polarization case, the electric field is transverse to the wave propagating direction, which in this case is y direction. Thus, E_z, H_x and H_y exist, with

$$\mathbf{E}(x,t) = E_z(x)e^{i(\omega t-\beta y)} \cdot \hat{a}_z \tag{14}$$

$$H_x = -\frac{\beta}{\omega\mu_o} E_z \tag{15}$$

$$H_y = -\frac{\beta}{j\omega\mu_o}\frac{\partial E_z}{\partial x} \tag{16}$$

The electric field expressions obtained by solving equations (11), (12) and (13) and applying the continuity condition of E_z at the interfaces are

$$E_z(x) = \begin{cases} Ce^{-qx} & 0 < x \\ C\left[\cos(hx) - \frac{q}{h}\sin(hx)\right] & -t \le x \le 0 \\ C\left[\cos(ht) + \frac{q}{h}\sin(ht)\right]e^{p(x+t)} & x < -t \end{cases} \tag{17}$$

where C is a constant that relates to the finite energy in the guided-wave, t is the thickness of the waveguide, and p, q and h are given by

$$q = \sqrt{\beta^2 - k_o^2 n_c^2} \tag{18}$$

$$h = \sqrt{k_o^2 n_g^2 - \beta^2} \tag{19}$$

$$p = \sqrt{\beta^2 - k_o^2 n_s^2} \tag{20}$$

These expressions reflect the field distribution for a guided-wave in each of the three different regions of figure 1. The propagation constant β is called the eigen value, and can be determined by applying continuity condition to the magnetic field component E_z at x = -t,

$$\tan(ht) = \frac{q + p}{h - \frac{q \cdot p}{h^2}}. \tag{21}$$

From equation (21), only discrete values of h are allowed. Each h identifies a specific β, hence a specific mode.

For transverse magnetic (TM) mode, a magnetic field does not exist along the wave propagating direction, and the existing field factors can be written as

$$\mathbf{H}(x,t) = H_z(x) e^{i(\omega t - \beta y)} \cdot \hat{a}_z \tag{22}$$

$$E_x = -\frac{\beta}{\omega \varepsilon_o n^2} H_z \tag{23}$$

$$E_y = -\frac{\beta}{j\omega \varepsilon_o n^2} \frac{\partial H_z}{\partial x}. \tag{24}$$

Similar to the TE-polarization case, the field distribution can be expressed as

$$H_z(x) = \begin{cases} C' e^{-qx} & x > 0 \\ C' \left[\cos(hx) - \frac{q}{h} \sin(hx) \right] & -t \le x \le 0 \\ C' \left[\cos(ht) + \frac{q}{h} \sin(ht) \right] e^{p(x+t)} & x < -t \end{cases} . \qquad (25)$$

The continuity conditions of the fields at the interfaces, in this case, produce the following eigen value expression for TM-polarization

$$\tan(ht) = \frac{\left(\frac{n_g}{n_s}\right)^2 q + \left(\frac{n_g}{n_c}\right)^2 p}{h - \left(\frac{n_g^2}{n_c n_s}\right)^2 \frac{q \cdot p}{h^2}} . \qquad (26)$$

The number of allowed eigen values (β) depends on n_g, n_c, n_s, t, and λ_o. Generally, a single mode is desirable in guided wave optics, which is the lowest order mode.

C. Optical Indicatrix in Uniaxial Crystals

An isotropic medium has a constant scalar dielectric susceptibility that is independent from the direction of the applied electric filed on the medium. Thus, the polarization density and the electric displacement vectors in the material are in the same direction as the applied electric field. On the other hand, if the medium is anisotropic, the dielectric susceptibility is not a scalar quantity but a tensor. Thus, the polarization density and the electric displacement vectors are not necessarily in the direction of the applied electric field. Lithium niobate is an anisotropic dielectric material.

For a non-magnetic anisotropic dielectric medium, the relative permittivities, hence the dielectric susceptibility as well, are expressed in 3x3 matrix form. To simplify analyses, a reference coordinate is selected to be identical coincide with the principal axes of the crystal. This makes the off-diagonal elements of the matrix vanish, and allows expressing the permittivity as

$$\begin{pmatrix} \varepsilon_{11} & 0 & 0 \\ 0 & \varepsilon_{22} & 0 \\ 0 & 0 & \varepsilon_{33} \end{pmatrix} = \varepsilon_o \begin{pmatrix} n_x^2 & 0 & 0 \\ 0 & n_y^2 & 0 \\ 0 & 0 & n_z^2 \end{pmatrix} \tag{27}$$

where ε_{11}, ε_{22}, ε_{33} are called principal permittivities. Substituting equation (27) into equation (5), the relation between electric field intensity vector **E** and displacement vector **D** can be expressed as

$$\mathbf{D} = \varepsilon \mathbf{E} = \begin{pmatrix} \varepsilon_{11} & 0 & 0 \\ 0 & \varepsilon_{22} & 0 \\ 0 & 0 & \varepsilon_{33} \end{pmatrix} \begin{pmatrix} E_x \\ E_y \\ E_z \end{pmatrix} \tag{28}$$

$LiNbO_3$ has a uniaxial crystal symmetry with $n_x = n_y \neq n_z$ which is the simplest anisotropic case. Utilizing the expression of the electric energy density of propagating wave in a crystal

$$U_e = \frac{1}{2} \mathbf{D} \cdot \mathbf{E} \tag{29}$$

and making use of equation (28) yield

$$U_e = \frac{1}{2}\left(\varepsilon_{11} E_x^2 + \varepsilon_{22} E_y^2 + \varepsilon_{33} E_z^2\right) = \frac{1}{2}\left(\frac{D_x^2}{\varepsilon_{11}} + \frac{D_y^2}{\varepsilon_{22}} + \frac{D_z^2}{\varepsilon_{33}}\right). \tag{30}$$

Defining $x = D_x \Big/ \sqrt{2U_e\varepsilon_o}$, $y = D_y \Big/ \sqrt{2U_e\varepsilon_o}$, and $z = D_z \Big/ \sqrt{2U_e\varepsilon_o}$, and recalling $\varepsilon = \varepsilon_o \cdot \varepsilon_r = \varepsilon_o \cdot n^2$, the above reduces to

$$\frac{x^2}{n_x^2} + \frac{y^2}{n_y^2} + \frac{z^2}{n_z^2} = 1. \tag{31}$$

Equation (31) defines an index ellipsoid, also called the indicatrix, and is obtained by choosing the x, y, and z axes of the coordinate system to coincide with the principal axes of the crystal. Taking the z axis as the axis of symmetry, equation (31) becomes

$$\frac{x^2}{n_o^2} + \frac{y^2}{n_o^2} + \frac{z^2}{n_e^2} = 1. \tag{32}$$

Here, $n_x = n_y \equiv n_o$ is called the ordinary index of refraction, and $n_z \equiv n_e$ is called the extraordinary index of refraction. The z-axis is called the optic axis. The figure 3 shows the index ellipsoid.

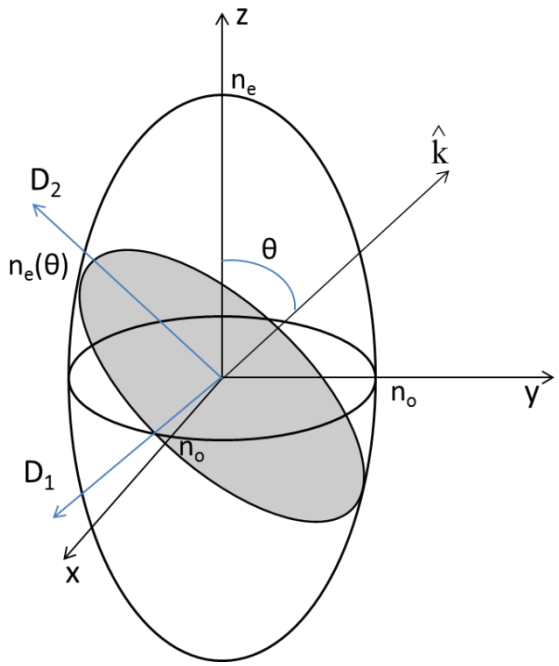

Fig. 3. The optical indicatrix of uniaxial crystals.

For an arbitrary propagation direction $\hat{k}$, an intersection plane with the index ellipsoid needs to be constructed. The intersection plane should include the origin of the index ellipsoid and be perpendicular to $\hat{k}$. The intersection plane is the ellipse shown in shade in figure 3. The major and minor axes of the ellipse identify the two allowed orthogonal directions of the displacement vector **D** associated with this wave. One allowed polarization is along D_1, and it is always constant because the minor axis is on the circle in the xy plane. The index along this axis is called the ordinary refractive index, n_o, and it is independent of the propagation direction. On the other hand, the other allowed polarization is D_2, and it depends on the angle θ. The index along this axis is called the extraordinary refractive index, $n_e(\theta)$, and is expressed as

$$\begin{aligned} n_e^2(\theta) &= y^2 + z^2 \\ y &= n_e(\theta)\cos\theta \\ z &= n_e(\theta)\sin\theta \end{aligned} . \tag{33}$$

$n_e(\theta)$ can be solved by substituting equation (33) into equation (32), and the solution is

$$n_e(\theta) = \frac{n_e n_o}{\sqrt{n_e^2 \cos^2\theta + n_o^2 \sin^2\theta}} . \tag{34}$$

If the wave propagates along the z direction, θ is zero. This causes $n_e(\theta) = n_o$ and the medium behave as if it is isotropic. This is why z axis is called the optic axis.

D. Linear Electro-Optic Effect

The linear electro-optic effect, also known as Pockels effect, refers to changes in the refractive indices of a dielectric crystalline material which can be induced by the application of an electric field and that are linearly proportional to the applied field. Depending on the orientation of the crystal axes and the direction of the applied electric field, it could also lead to rotation of the index ellipsoid. The Pockels effect in $LiNbO_3$ is strong due to its good electro-optic properties.

When electric field is applied, the index ellipsoid of an anisotropic crystal is modified according to

$$\left(\frac{1}{n_1^2}\right)x^2 + \left(\frac{1}{n_2^2}\right)y^2 + \left(\frac{1}{n_3^2}\right)z^2 + 2\left(\frac{1}{n_4^2}\right)yz + 2\left(\frac{1}{n_5^2}\right)xz + 2\left(\frac{1}{n_6^2}\right)xy = 1 . \tag{35}$$

For an applied electric field, the extent of these modifications depends largely on the

values of the electro-optic coefficient tensor elements (γ_{ij}) of the material. The refractive index changes induced by an applied electric field is given by

$$\Delta\left(\frac{1}{n_i^2}\right) = \sum_{j=1}^{3} \gamma_{ij} E_j \qquad i=1,2,\ldots,6. \tag{36}$$

The electro-optic tensor for $LiNbO_3$ is

$$\begin{pmatrix} 0 & -\gamma_{22} & \gamma_{13} \\ 0 & \gamma_{22} & \gamma_{13} \\ 0 & 0 & \gamma_{33} \\ 0 & \gamma_{51} & 0 \\ \gamma_{51} & 0 & 0 \\ -\gamma_{22} & 0 & 0 \end{pmatrix} \tag{37}$$

where $\gamma_{22} = 3.4 \times 10^{-12}$ m/V, $\gamma_{13} = 8.6 \times 10^{-12}$ m/V, $\gamma_{33} = 30.8 \times 10^{-12}$ m/V and $\gamma_{51} = 28 \times 10^{-12}$ m/V [22]. Since $LiNbO_3$ is uniaxial material, $n_x = n_y \equiv n_o$ and $n_z \equiv n_e$. For an electric field applied parallel to the crystal y-axis, $\mathrm{E}^{\mathrm{e}} = E_y \hat{a}_y$, the refractive indices becomes

$$\frac{1}{n_x^2} = \frac{1}{n_o^2} - \gamma_{22} E_y \tag{38}$$

$$\frac{1}{n_y^2} = \frac{1}{n_o^2} + \gamma_{22} E_y \tag{39}$$

$$\frac{1}{n_z^2} = \frac{1}{n_e^2}. \tag{40}$$

Eventually, this reduces equation (35) to

$$\left(\frac{1}{n_o^2} - \gamma_{22} E_y\right) x^2 + \left(\frac{1}{n_o^2} + \gamma_{22} E_y\right) y^2 + \frac{1}{n_e^2} z^2 + 2(\gamma_{51} E_y) yz = 1. \tag{41}$$

In equation (41), the mixed component does not include x-axis. Therefore, the rotation of the index ellipsoid is about the x-axis in y-z plane.

E. TE-TM Mode Conversion and Phase Shift

For waveguides that are produced in electro-optic materials, if a guided mode experiences periodic perturbations in refractive index, mode conversion between TE and TM polarization occurs. The coupled-mode theory helps explain this phenomenon as being related to perturbations of charge distribution in the waveguide that are experienced by the propagating wave. From equation (7), the wave equation for a guided mode in a waveguide can be expressed as

$$\nabla^2 \mathbf{E}(r,t) = \varepsilon(r)\mu_0 \frac{\partial^2 \mathbf{E}(r,t)}{\partial t^2}. \tag{42}$$

Substituting equation (5) into (42), and utilizing the relation $\varepsilon(r)\mathbf{E}(r,t) = \mathbf{P}(r,t) + \varepsilon_0 \mathbf{E}(r,t)$ gives

$$\nabla^2 \mathbf{E}(r,t) = \varepsilon_o \mu_o \frac{\partial^2 \mathbf{E}(r,t)}{\partial t^2} + \mu_o \frac{\partial^2 \mathbf{P}(r,t)}{\partial t^2}. \tag{43}$$

The dielectric polarization surface charge density vector **P** can be separated into perturbed and unperturbed terms

$$\mathbf{P}(r,t) = \mathbf{P_o}(r,t) + \mathbf{P_{pert}}(r,t) \tag{44}$$

$$\mathbf{P_o}(r,t) = \left[\varepsilon(r) - \varepsilon_o\right]\mathbf{E}(r,t). \tag{45}$$

$$\nabla^2 \mathbf{E}(r,t) - \mu_o \varepsilon(r) \frac{\partial^2 \mathbf{E}(r,t)}{\partial t^2} = \mu_o \frac{\partial^2}{\partial t^2} \mathbf{P_{pert}}(r,t) \tag{46}$$

$$D_i = \varepsilon_{ij} E_j = \varepsilon_o E_i + P_i \tag{47}$$

$$P_i = \left(\varepsilon_{ij} - \varepsilon_o \delta_{ij}\right) E_j \tag{48}$$

where δ_{ij}=1 for i=j, and 0 for i≠j.

$$\left[P_{pert}\right]_i = \Delta P_i = \Delta\varepsilon_{ij} E_j = \varepsilon_o \left(\varepsilon_{ij}^{'}\right) E_j \tag{49}$$

$$\left[P_{pert}\right]_i = \Delta P_i = -\varepsilon_o \varepsilon_{ii}^{'} \varepsilon_{jj}^{'} \Delta\left(\frac{1}{n^2}\right)_{ij} E_j \tag{50}$$

In an x-cut, y-propagating $LiNbO_3$ waveguide, TE polarization has a transverse electric field along z-axis, i.e. $E_z \neq 0$, $E_x = 0$. For TE→TM mode conversion, a polarization perturbation along x-axis, P_x, is required, and it can be expressed as

$$\Delta P_x = -\varepsilon_o \varepsilon_{11}^{'} \varepsilon_{33}^{'} \Delta\left(\frac{1}{n^2}\right)_{13} E_z = -\varepsilon_o n_o^2 n_e^2 \Delta\left(\frac{1}{n^2}\right)_5 E_z \tag{51}$$

where $\varepsilon_{11}^{'} = n_o^2$ and $\varepsilon_{33}^{'} = n_e^2$ for a uniaxial crystal.

On the other hand, TM polarization has a transverse electric field along x-axis, i.e. $E_x \neq 0$, $E_z = 0$. A polarization perturbation along z-axis is required, P_z, for TM→TE mode conversion, and it can be expressed as

$$\Delta P_z = -\varepsilon_o n_o^2 n_e^2 \Delta\left(\frac{1}{n^2}\right)_5 E_x \tag{52}$$

As shown in equation (51) and (52), TE↔TM conversion utilizes Δn_5, which can be induced by electro-optic effect.

Coupled-mode equation establishes the relation between two orthogonal coupled modes, and is expressed by

$$\frac{dA_{TE}}{dy} = -j\kappa_o B_{TM}(y)e^{-j\Delta\beta y} \tag{53}$$

$$\frac{dB_{TM}}{dy} = -j\kappa_o A_{TE}(y)e^{j\Delta\beta y} \tag{54}$$

where $\Delta\beta = \beta_{TE} - \beta_{TM} = \frac{2\pi}{\lambda_o}(n_e - n_o)$ represents a phase mismatch factor, and $\kappa_o = \frac{\pi}{\lambda}(n_o n_e)^{3/2}\gamma_{51}E_x^e$ is the coupling coefficient. β_{TE} and β_{TM} are the propagating constant of TE mode and TM, respectively. A_{TE} and B_{TM} are the amplitude of TE mode and TM mode, respectively. Solutions of the coupled equations (53) and (54) subject to boundary conditions yield expressions for TE and TM amplitude variation along the direction of propagation. If a TE mode is incident, i.e. $A(0)=1$, $B(0)=0$, the solutions are

$$A_{TE}(y) = e^{-j\Delta y/2}\left(\cos\delta y + j\frac{\Delta}{2\delta}\sin\delta y\right) \tag{55}$$

$$B_{TM}(y) = -j\frac{\kappa}{\delta}e^{j\Delta y/2}\sin\delta y \tag{56}$$

where $\delta = \sqrt{\kappa^2 + \left(\frac{\Delta}{2}\right)^2}$.

With a phase-matched condition $\Delta = 0$, which can occur at a specific wavelength and ignore losses, all electric field of TE mode can be coupled into TM mode. However, the phase-mismatch factor (Δ) cannot be zero at other wavelengths, as such a partial

transfer of the field occurs. The phase-matched condition for the given optical frequency is given by

$$\Delta = \frac{2\pi\nu}{c}\left(n_e - n_o\right) \pm \frac{2\pi}{\Lambda} \tag{57}$$

where ν is the phase matched optical frequency, *c* is the speed of light, and Λ is the period of perturbation for the phase-matched condition

$$\Lambda = \frac{c}{\nu_o\left(n_e - n_o\right)} = \frac{\lambda_o}{\left|n_o - n_e\right|} \tag{58}$$

In equation (58), λ_o is the wavelength corresponding to frequency ν_o. A phase-matched condition highly depends on the selected wavelength, so for a given period the condition can be changed by modifying a birefringence $|n_o - n_e|$. If random optical wave is coupled into a polarization converter, that wave can be decomposed into TE and TM polarization components, and then the output wave is obtained by adding both components. The transfer matrix of a polarization converter can be expressed as (59)

$$M_c = \begin{pmatrix} e^{-j\Delta y/2}\left(\cos\delta y + j\frac{\Delta}{2\delta}\sin\delta y\right) & -j\frac{\kappa}{\delta}e^{j\Delta y/2}\sin\delta y \\ -j\frac{\kappa}{\delta}e^{-j\Delta y/2}\sin\delta y & e^{j\Delta y/2}\left(\cos\delta y - j\frac{\Delta}{2\delta}\sin\delta y\right) \end{pmatrix}. \tag{59}$$

For a given incident polarization as an input into a converter, the output can be expressed as a multiplication of input amplitudes column vector and the transfer matrix of the polarization converter.

As mentioned previously the change on the refractive index induced by an applied electric field affects the propagation of a guided wave. Assuming 45^o polarized wave is propagating in a waveguide, the phase accumulated through a travel length ℓ by

the TE and TM polarization components caused from the intrinsic natural birefringence of the waveguide material is

$$\phi_{TM} = \left(\frac{2\pi}{\lambda_o} n_e\right)\ell \tag{60}$$

$$\phi_{TE,\ell} = \left(\frac{2\pi}{\lambda_o} n_o\right)\ell . \tag{61}$$

The intrinsic phase difference can be expressed as

$$\Delta\phi_\ell = \frac{2\pi}{\lambda_o}(n_e - n_o)\ell \tag{62}$$

When an electric field is applied along z-axis of the crystal, i.e. $E^e = E_z^e \hat{a}_z$ over a length ℓ along the y-direction of the crystal, the refractive index becomes

$$n_e^{'} = n_e + \frac{1}{2} n_e^3 \gamma_{33} E_z^e \tag{63}$$

$$n_o^{'} = n_o + \frac{1}{2} n_o^3 \gamma_{13} E_z^e , \tag{64}$$

and the electro-optically induced phase for TM is

$$\Delta\phi_{TM}^e = \frac{\pi}{\lambda_o} n_e^3 \gamma_{33} E_z^e \ell . \tag{65}$$

Similarly, the electro-optically induced phase for TE polarization is

$$\Delta\phi_{TE}^e = \frac{\pi}{\lambda_o} n_o^3 \gamma_{13} E_z^e \ell . \tag{66}$$

The electro-optically induced phase retardation between two polarizations can then be expressed as

$$\delta\phi = \frac{\pi}{\lambda_o}\left[\left(n_e^3\gamma_{33} - n_o^3\gamma_{13}\right)E_z^e\right]\ell\,. \tag{67}$$

This results in the total phase retardation of

$$\Delta\phi = \Delta\phi_\ell + \delta\phi\,. \tag{68}$$

Finally, a transfer matrix for a phase shifter can be expressed as

$$M_S = \begin{pmatrix} e^{-j\Delta\phi/2} & 0 \\ 0 & e^{j\Delta\phi/2} \end{pmatrix}. \tag{69}$$

Thus, by applying an electric field, the total phase difference, $\Delta\phi$, between the TE mode and the TM mode, equation (69), can be adjusted.

F. Polarization Control

Polarization is a common property of an optical wave, but it becomes a crucial factor in optical signal processing. As optical wave is transmitted through an optical fiber network, optical wave experiences polarization dependent loss (PDM) or polarization mode dispersion (PMD), which are the typical polarization-related issues [11]. Since these issues distort information transmitted via optical waves, polarization control technique has been employed.

The Poincare sphere is well-known analysis plot to explain state of polarizations (SOP). Figure 4 describes the Poincare sphere. Each point on the sphere surface represents each different state of polarization. S_1, S_2 and S_3 are components constructing

the sphere are. They are called the Stoke vectors, and they are explained in equation (70) for a polarized light with a complex representation $\chi = e^{i\delta} \tan\psi$ [23].

$$S = \begin{pmatrix} S_o \\ S_1 \\ S_2 \\ S_3 \end{pmatrix} = \begin{pmatrix} 1 \\ \cos 2\psi \\ \sin 2\psi \cos\delta \\ \sin 2\psi \sin\delta \end{pmatrix} \tag{70}$$

Each end of axes represents unique SOPs. The circular boundary of the S_1-S_2 plane represents linear polarization state. Especially, the (S_1, S_2, S_3) coordinate of (1, 0, 0), which is front end of S_1 axis, is horizontal linear polarization, and (-1, 0, 0) represents vertical linear polarization, and S2 axis represents 45^o from the x-axis. Meanwhile the ends (0, 0, 1) or (0, 0, -1) of S_3 axis are corresponds to circular polarizations [23].

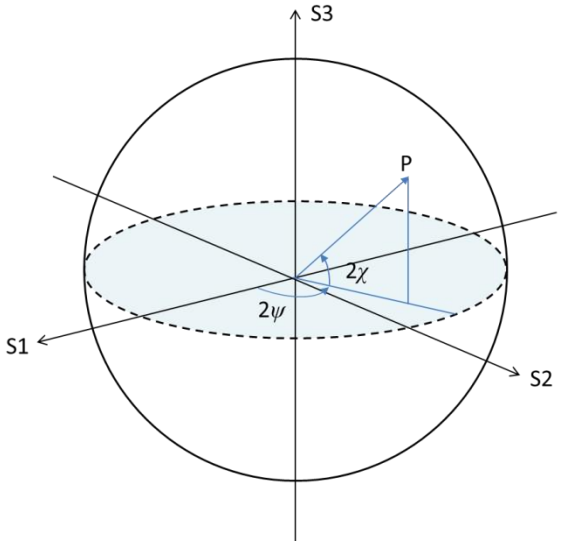

Fig. 4. The Poincare sphere.

To determine the polarization state, the point (P) on the sphere should be projected on S_1-S_2 plane. On the plane, the deviation angle from S1 axis corresponds to a double of the polarization angle (ψ), and the vertical angle from the plane to the point P represents a double of the phase angle (χ) of the polarization state.

Typical polarization controllers consist of two quarter-wave plates (QWPs) and one half-wave plate (HWP) placed between two QWPs. It provides a mean to induce polarization changes from random input state to arbitrary output state. A QWP and HWP can be expressed by Jones Matrix.

$$M_q = \begin{pmatrix} \cos\alpha & -\sin\alpha \\ \sin\alpha & \cos\alpha \end{pmatrix} \qquad \text{for QWP} \tag{71}$$

$$M_h = \begin{pmatrix} e^{i\beta} & 0 \\ 0 & e^{-i\beta} \end{pmatrix} \qquad \text{for HWP} \tag{72}$$

In polarization control, the first QWP typically changes any input polarization states to linear polarization, and HWP plays a role to rotate a polarization angle of linear polarization [26]. Then, the second QWP is able to change polarization state [26]. In this manner, polarization control to any intended states of polarization can be available.

CHAPTER III

DEVICE STRUCTURE AND ANALYSIS

In this chapter, the structure of the suggested device is presented. It consists of two polarization converters with a phase shifter between them. Using the described matrix representation of these elements from the previous chapter, the behavior of the polarization converter and phase shifter are briefly summarized first individually. Then the behavior of a randomly polarized incident wave as it is guided by the channel waveguide through the integrated elements for its output polarization control is described.

A. Device Configuration

A schematic of the device configuration is illustrated in figure 5. It includes two polarization converters near the ends of the sample, with a phase shifter centered between them. All the elements are integrated on a single channel waveguide. The substrate is x-cut y-propagating $LiNbO_3$, which is an electro-optic birefringent crystalline material.

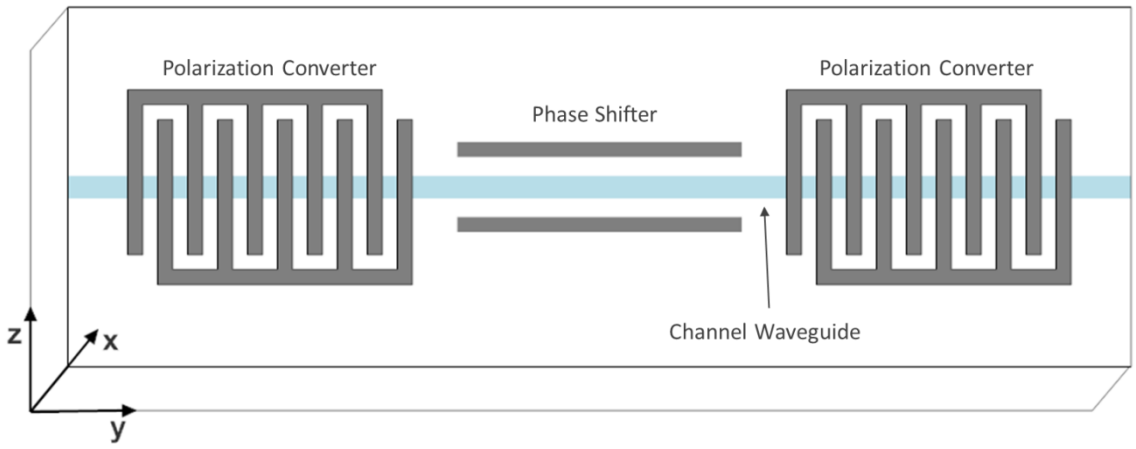

Fig. 5. Schematic structure of the device configuration with cascaded polarization converters and a phase shifter.

B. Polarization Converter

The polarization converter is a key element for controlling the polarization state of an optical wave. Its primary purpose is to rotate the polarization angle of an incident optical wave, most commonly between the orthogonal TE and TM polarizations. A rotation of the polarization angle of the guided wave requires coupling between orthogonal components, and can be achieved by periodic perturbation of the refractive index along the propagation direction which can be realized by electro-optic perturbations as described. Polarization converters utilizing the electro-optic effect have been investigated for decades [24].

Figure 6 displays the schematic structure of the polarization converter electrode set used in this research. It is composed of inter-digitized electrodes with a multiple number of the period of Λ over a total length L_c for the coupling region.

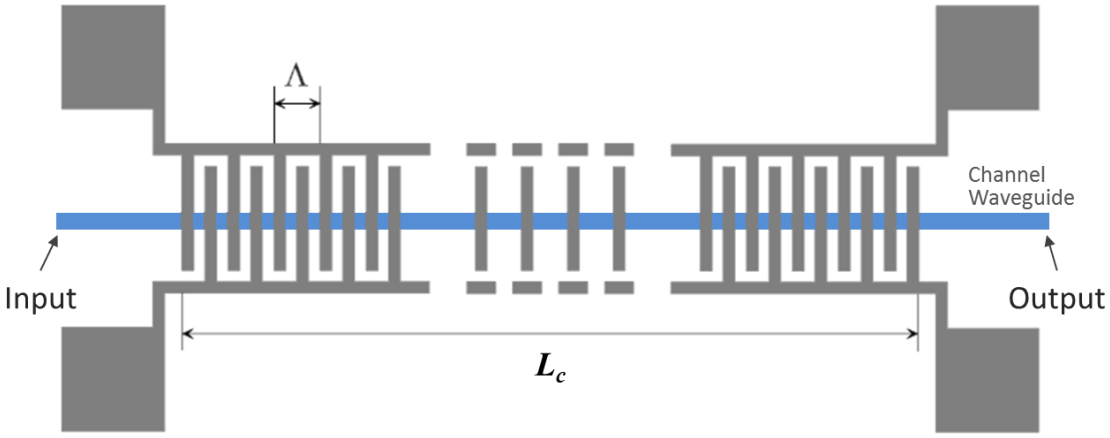

Fig. 6. Schematic structure of the polarization converter electrode set on a channel waveguide.

As a guided wave propagates, each period of the electrode induces perturbation on the electric field components of the optical wave. The large number of the period promotes additive rotation, and reduces voltage requirements for 90^o rotation. On the other hand, this increases the sample length. The amplitudes of the output orthogonal field components for an optical wave that passes through the converter can be expressed by multiplying the transfer matrix of the polarization converter M_c (equation 59) with the amplitudes of the orthogonal field components of the input optical wave (A_{in}).

$$\begin{pmatrix} A_{TE}(L_c) \\ A_{TM}(L_c) \end{pmatrix} = M_c \cdot A_{in}$$

$$= \begin{pmatrix} e^{-j\Delta L_c/2}\left(\cos\delta L_c + j\frac{\Delta}{2\delta}\sin\delta L_c\right) & -j\frac{\kappa}{\delta}e^{j\Delta L_c/2}\sin\delta L_c \\ -j\frac{\kappa}{\delta}e^{-j\Delta L_c/2}\sin\delta L_c & e^{j\Delta L_c/2}\left(\cos\delta L_c - j\frac{\Delta}{2\delta}\sin\delta L_c\right) \end{pmatrix} \begin{pmatrix} A_{TE}(0) \\ A_{TM}(0) \end{pmatrix}. \quad (73)$$

Equation (73) represents the variations experienced by the orthogonal components of a wave as it passes through a converter of length L_c. The terms Δ and δ are related to phase mismatch in the optical spectral frequency, and described earlier in equations (56) and (57). $A_{TE}(0)$ is the amplitude of the TE component at the input, and $A_{TM}(0)$ is the amplitude of the TM component. $A_{TE}(L_c)$ and $A_{TM}(L_c)$ are the amplitudes of the orthogonal polarization at the output, respectively. κ is the coupling coefficient per unit length. The rotation angle of the polarization of the optical wave depends on the value of κL.

C. Phase Shifter

The phase shifter provides a means for modifying the retardation between the TE and TM polarization components of a guided wave. In this work, the phase shifter is inserted between the two electro-optic polarization converters, to control the retardation at the input of the second converter. In a separate investigation, this configuration is extended for integration with a chalcogenide ring resonator [25]. For the used substrate orientation (x-cut, y-propagation), the phase shifter is formed by delineating two parallel surface electrodes centered along the channel waveguide. The structure of the phase shifter with electrode length L_s is illustrated in figure7.

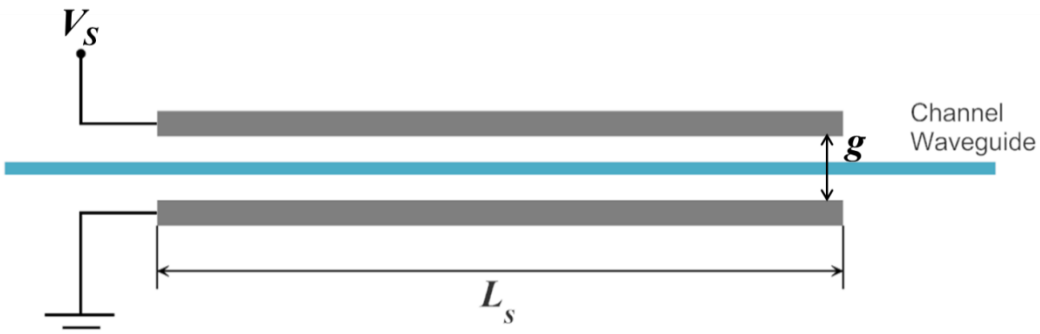

Fig. 7. The schematic structure of the phase shifter electrodes set.

The total retardation between two converters can be determined by including the contribution from electro-optically induced phase retardation, described in equation (67) of chapter 2, with the intrinsic retardation inherent in the birefringence of the material. The electric field (E_z) across the channel waveguide can be approximated by dividing the applied voltage (V_s) on the electrodes by the gap (g) between them. The electro-optically induced phase retardation can then be estimated by

$$\delta\phi_{L_s} = \frac{\pi}{\lambda_o}\left[\left(n_e^3\gamma_{33} - n_o^3\gamma_{13}\right)\frac{V_s}{g}\alpha\right]L_s \tag{74}$$

where α is the overlap factor between optical and applied electrical fields. The intrinsic phase retardation between the two converters which must be added to the induced retardation of the phase shifter can be determined from equation (62) with the length of L_3, shown in figure 8. This results in the total phase retardation for the segment between the two converters, which may be expressed simply as

$$\Delta\phi_s = \Delta\phi_{L_3} + \delta\phi_{L_s}\,. \tag{75}$$

Substituting expression (75) for $\Delta\phi$ in equation (69), the transfer matrix for the total phase shift between the orthogonal components along the segment between the two converters can be represented as

$$M_S = \begin{pmatrix} e^{-j\Delta\phi_s/2} & 0 \\ 0 & e^{j\Delta\phi_s/2} \end{pmatrix}. \tag{76}$$

D. Overall Integrated Device Behavior

The behavior of the overall integrated device (Fig. 5) can be analyzed by decomposing it into three regions as shown in figure 8, and using matrix multiplication to describe the variations experienced by an incident optical wave as it travels through each region at the phase matched wavelength.

The transfer matrix of the overall device (M_T) can be expressed by the product of the transfer matrix of each element in reverse order,

$$M_T = M_{C2} \cdot M_S \cdot M_{C1}. \tag{77}$$

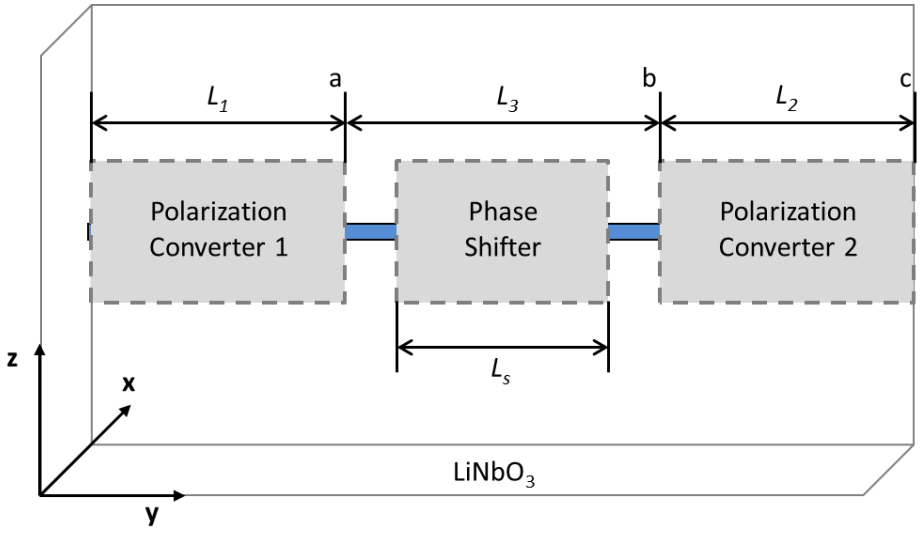

Fig. 8. The block diagram of the device.

For an incident wave at the phase-matched wavelength, the output from the first converter (point 'a' in Fig. 8) given in equation (73) can be simplified by setting the phase-mismatch factor (Δ) to zero, yielding

$$\begin{pmatrix} A_{TE}(L_1) \\ A_{TM}(L_1) \end{pmatrix} = M_{c1} \cdot A_{in} = \begin{pmatrix} \cos \kappa L_{c1} & -j \sin \kappa L_{c1} \\ -j \sin \kappa L_{c1} & \cos \kappa L_{c1} \end{pmatrix} \begin{pmatrix} A_{TE}(0) \\ A_{TM}(0) \end{pmatrix}. \tag{78}$$

If the incident wave entering the device at the input of the sample is polarized at an angle (θ_i), the electric field amplitudes for the orthogonal components at the input of the first converter can be expressed as $A_{TE}(0) = |A_o| \cos \theta_i$ and $A_{TM}(0) = |A_o| \sin \theta_i \cdot e^{j\phi_i}$, where A_o is the amplitude of the electric field for the incident wave at the input of the device and ϕ_i is the relative phase delay between the orthogonal field components caused by the inherent birefringence of the substrate material. The output electric field

amplitudes of the first polarization converter for the phase matched wavelength at point 'a' in figure 8 can then be determined from equation (78) and expressed as

$$A_{out1} = \begin{pmatrix} A_{TE,out} \\ A_{TM,out} \end{pmatrix} = |A_o| \begin{pmatrix} \left(\cos \kappa_1 L_{c1} \cdot \cos \theta_i - j e^{j\phi_i} \sin \kappa_1 L_{c1} \cdot \sin \theta_i\right) \\ \left(-j \sin \kappa_1 L_{c1} \cdot \cos \theta_i + e^{j\phi_i} \cos \kappa_1 L_{c1} \cdot \sin \theta_i\right) \end{pmatrix}. \qquad (79)$$

In the above equation, A_{out1} denotes the vector field at the output of the first converter, L_{c1} and κ_1 are the coupling length and the coupling coefficient of the first polarization converter, respectively.

The optical wave coming out of the first converter region (point 'a' in Fig. 8) then traverses the center region and continues toward the second converter. During the travel, its orthogonal components accumulate additional phase shift relative to each other due to contributions from the birefringence of the material over the center region length L_3, as well as electro-optically induced index changes over the phase shifter electrode length L_s. Since the phase contributions are additive, the two add up and the sum may be denoted as $\Delta\phi_s$. Thus, the amplitudes of the orthogonal components for the optical wave (A_{out2}) at point 'b' can be determined by multiplying equation (79) with equation (76), which is the transfer matrix of the center region. Hence

$$A_{out2} = \begin{pmatrix} e^{-j\Delta\phi_s/2} & 0 \\ 0 & e^{j\Delta\phi_s/2} \end{pmatrix} A_{out1}$$

$$= \begin{pmatrix} A_{TE,out} \\ A_{TM,out} \end{pmatrix} = |A_o| \begin{pmatrix} e^{-j\Delta\phi_s/2}\left(\cos \kappa_1 L_{c1} \cdot \cos \theta_i - j e^{j\phi_i} \sin \kappa_1 L_{c1} \cdot \sin \theta_i\right) \\ e^{j\Delta\phi_s/2}\left(-j \sin \kappa_1 L_{c1} \cdot \cos \theta_i + e^{j\phi_i} \cos \kappa_1 L_{c1} \cdot \sin \theta_i\right) \end{pmatrix}. \qquad (80)$$

As the optical wave continues its travel through the second converter region form point 'b' toward point 'c' in figure 8, it undergoes similar coupling and retardation effects as of the first converter.

Following similar steps as before, the amplitude of the orthogonal components at the output of the second converter region, A_{out3} (point 'c' in Fig. 8) can be expressed as

$$A_{out3} = M_{c2} \cdot A_{out2}$$

$$= |A_o| \begin{pmatrix} e^{-j\Delta\phi_s/2}\left(\cos\kappa_2 L_{c2}\left(\cos\kappa_1 L_{c1}\cdot\cos\theta_i - je^{j\phi_i}\sin\kappa_1 L_{c1}\cdot\sin\theta_i\right)\right) \\ \qquad + e^{j\Delta\phi_s/2}\left(\sin\kappa_2 L_{c2}\left(-\sin\kappa_1 L_{c1}\cdot\cos\theta_i - je^{j\phi_i}\cos\kappa_1 L_{c1}\cdot\sin\theta_i\right)\right) \\ e^{-j\Delta\phi_s/2}\left(-j\sin\kappa_2 L_{c2}\left(\cos\kappa_1 L_{c1}\cdot\cos\theta_i - je^{j\phi_i}\sin\kappa_1 L_{c1}\cdot\sin\theta_i\right)\right) \\ \qquad + e^{j\Delta\phi_s/2}\left(\cos\kappa_2 L_{c2}\left(-j\sin\kappa_1 L_{c1}\cdot\cos\theta_i + e^{j\phi_i}\cos\kappa_1 L_{c1}\cdot\sin\theta_i\right)\right) \end{pmatrix}. \tag{81}$$

Here, κ_2 and L_{c2} are the second converter coupling coefficient and length, respectively. Carrying out the multiplication of matrices, yields the final expressions for the orthogonal components at the output of the device (point 'c' in Fig. 8)

$$A_{TE}^{final} = |A_o|\left(e^{-j\Delta\phi_s/2}\left(\cos\kappa_2 L_{c2}\left(\cos\kappa_1 L_{c1}\cdot\cos\theta_i - je^{j\phi_i}\sin\kappa_1 L_{c1}\cdot\sin\theta_i\right)\right) + e^{j\Delta\phi_s/2}\left(\sin\kappa_2 L_{c2}\left(-\sin\kappa_1 L_{c1}\cdot\cos\theta_i - je^{j\phi_i}\cos\kappa_1 L_{c1}\cdot\sin\theta_i\right)\right)\right) \tag{82-a}$$

$$A_{TM}^{final} = |A_o|\left(e^{-j\Delta\phi_s/2}\left(-j\sin\kappa_2 L_{c2}\left(\cos\kappa_1 L_{c1}\cdot\cos\theta_i - je^{j\phi_i}\sin\kappa_1 L_{c1}\cdot\sin\theta_i\right)\right) + e^{j\Delta\phi_s/2}\left(\cos\kappa_2 L_{c2}\left(-j\sin\kappa_1 L_{c1}\cdot\cos\theta_i + e^{j\phi_i}\cos\kappa_1 L_{c1}\cdot\sin\theta_i\right)\right)\right) \tag{82-b}$$

For the special case of a TE-polarized incident wave, θ_i is zero, ϕ_i vanishes, and for simplicity of notation A_o may be assumed to be one. To equally divide power into two by the electro-optically induced coupling through the first converter, the applied voltage on it can be adjusted to make $\kappa_1 L_{c1} = \pi/4$ in equation (81). This produces TE and TM components of equal amplitudes. Under ideal conditions, the two polarization converters are intended to be identical. This means both will have the same value for the phase-matched wavelength, and will require equal voltage values to achieve same amount of conversion (rotation) through each. Hence, the voltage on the second converter can also be adjusted to make $\kappa_2 L_{c2} = \pi/4$. Thus all the terms cos($\kappa_i L_{Ci}$) and sin($\kappa_i L_{Ci}$) with i = 1, 2 (in Eq. (81)) reduce to $\sqrt{2}/2$. Equations (82-a) and (82-b) in this case reduce to

$$A_{TE}^{final} = e^{-j\Delta\phi'/2}\left(\frac{1}{2} - e^{j\Delta\phi'}\frac{1}{2}\right) \tag{83-a}$$

$$A_{TM}^{final} = e^{-j\Delta\phi'/2}\left(-j\frac{1}{2} - je^{j\Delta\phi'}\frac{1}{2}\right) \tag{83-b}$$

In addition, if a voltage is applied on the phase-shifter in the center region, then $\Delta\phi_s$ could also be controlled. When the applied voltage is adjusted to make $\Delta\phi_s$ = m(2π) with m = 0, 1, 2, …; equations (83-a) and (83-b) reduce

$$for \quad \Delta\phi_s = (2m)\pi, \quad m = 0,\ 1\ ,2\ ,\ ... \begin{cases} A_{TE}^{final} = 0 \\ A_{TM}^{final} = 1\cdot e^{-j(2m+1)\pi/2} \end{cases} \tag{84}$$

On the other hand, if the applied voltage on the phase shifter makes $\Delta\phi_s = (2m+1)\pi$ with m = 0, 1, 2, …; equations (83-a) and (83-b) become

$$for \quad \Delta\phi_s = (2m+1)\pi, \quad m = 0 \;,1\;,2\;,\; ... \begin{cases} A_{TE}^{final} = 1 \cdot e^{-j(2m+1)\pi/2} \\ A_{TM}^{final} = 0 \end{cases} \tag{85}$$

If the separation length between the two converters L_3 is designed to maintain the retardation between the orthogonal components of the first converter output and the second converter input fixed at π/2, meaning no voltage will be required for equation (84) to be satisfied and minimum voltage for equation (85) to be satisfied, or simply m = 0. Equations (84) and (85) become

$$\Delta\phi' = 0 \qquad \begin{cases} A_{TE}^{final} = 0 \\ A_{TM}^{final} = -j \end{cases} \tag{86}$$

$$\Delta\phi' = \pi \qquad \begin{cases} A_{TE}^{final} = -j \\ A_{TM}^{final} = 0 \end{cases}$$

This behavior indicates that when the two converters are voltage tuned to produce equal split if incident intensity through each and by adjusting the voltage on the phase shifter, the polarization of the device output can be modulated between orthogonal TE and TM components for the phase-matched wavelength. Hence, if a bulk analyzer is placed on the output side of the sample and oriented in a direction normal to the polarization incident on the polarization that is incident on the device at its input, polarization intensity modulation can be obtained with an RF voltage on the phase shifter.

E. Polarization Controller

Several polarization controller configurations have been investigated. Among these, a structure with three retarders including two couplers was proposed by Noe [14]. Similar schemes have been proposed by other research [17, 26]. The transfer matrix for such structures can be represented as [17]

$$\begin{pmatrix} \cos\alpha & j\sin\alpha \\ j\sin\alpha & \cos\alpha \end{pmatrix}\begin{pmatrix} e^{j\beta} & 0 \\ 0 & e^{-j\beta} \end{pmatrix}\begin{pmatrix} \cos\gamma & j\sin\gamma \\ j\sin\gamma & \cos\gamma \end{pmatrix}. \tag{87}$$

α and γ represent the transformation angle of the polarization, and β is the retardation from birefringence. The above equation is similar to the transfer matrix expression of the device in this work

$$M_T = \begin{pmatrix} \cos\kappa_1 L_{c1} & -j\sin\kappa_1 L_{c1} \\ -j\sin\kappa_1 L_{c1} & \cos\kappa_1 L_{c1} \end{pmatrix}\begin{pmatrix} e^{-j\Delta\phi_s/2} & 0 \\ 0 & e^{j\Delta\phi_s/2} \end{pmatrix}\begin{pmatrix} \cos\kappa_2 L_{c2} & -j\sin\kappa_2 L_{c2} \\ -j\sin\kappa_2 L_{c2} & \cos\kappa_2 L_{c2} \end{pmatrix}. \tag{88}$$

Based on this analogy, the polarization control property of the device in this work was evaluated by simulation. As a polarization controller, the device must operate properly for any incident and desired output states of polarization. Figure 9 displays the simulation results on a Poincare sphere. The selected incident polarization angle was 56^{o} from the z-axis for this simulation. The Poincare sphere in figure 10 shows the entire surface is covered by the red simulated output points. This simulated plot asserts that the investigated device can also function as a polarization controller.

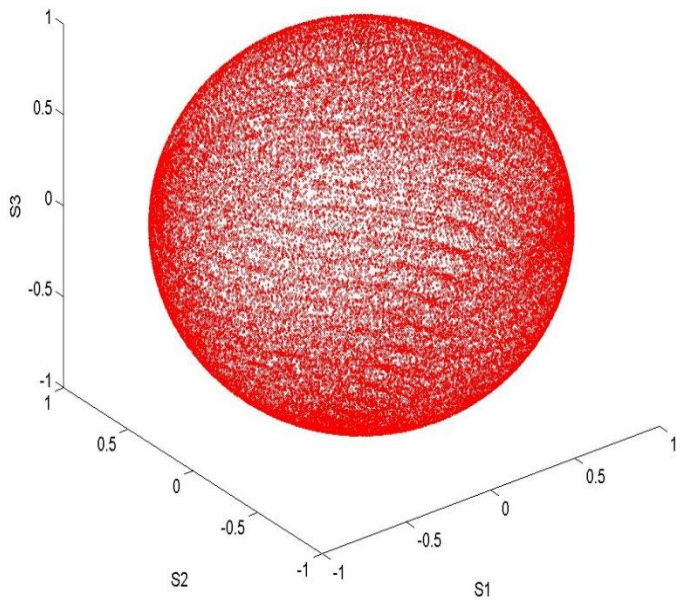

Fig. 9. The simulation result of the dynamic polarization controller for the input polarization of 56^{o} from x-axis.

CHAPTER IV

DEVICE FABRICATION

In this chapter, the fabrication process of the device is outlined. There are two crucial parts in the fabrication of the device. The first is the formation of the optical waveguide, and the second is the fabrication of the surface electrodes for inducing the desired electro-optic effects in the polarization converter and the phase shifter elements. Fabrication aspects that are critical to each are discussed.

A. Ti Diffused $LiNbO_3$ Waveguide

The titanium (Ti) diffused $LiNbO_3$ waveguide is a well-known method for optical waveguide fabrication. Commercial 3.0-in diameter 1.0-mm thick x-cut $LiNbO_3$ wafers from Crystal Technology Inc. (Palo Alto, CA) have been utilized in this research. To exploit the largest electro-optic coefficient, the y-axis of the crystal was adapted for the direction of propagating in the waveguides. Firstly, the $LiNbO_3$ wafers were cut with a dicing saw into 38 mm long (in y-axis direction) by 15 mm wide (in z-axis direction). The diced samples were cleaned by soapy water, then by organic solvents and De-Ionized (DI) water (Appendix I).

Next, Ti film was deposited on the surface of cleaned $LiNbO_3$ substrates via a DC magnetron sputtering system (AJA International Inc. Model : ATC ORION 5 UHV). After deposition, the thickness of the Ti film was measured by a Dektak surface profiler

using pad geometries that were delineated during the patterning stage of the Ti stripes for waveguides formation.

Channel waveguide patterns were delineated by photo lithography. The AZ-5214 photoresist (PR) from AZ Electronic Materials was spin-coated and exposed by an MA6 mask aligner (Appendix II). Then, the delineated PR patterns were developed in MF312 developer solution. Thermal curing in an oven for 15 minutes at 135 ^{o}C hardened the PR patterns enough to endure the etching process. Then, Reactive Ion Etching (RIE) was used to etch stripe channel waveguide patterns. The RIE process is a well-known dry etching plasma method capable of producing nearly vertical edges with very little distortion. The RIE process is anisotropic because ion plasma flows and collides with a substrate according to the direction of the electric field imposed in the process chamber. In this work, a mixture of fluoroform (CHF_3) gas and argon (Ar) gas was used for etching the Ti film (Appendix III). During the RIE helium (He) gas was also added to the chamber. He gas helps cool down and stabilize plasmas during the etching process [27]. If the duration of RIE process lasts too long, Ar^+ plasma can cause permanent mechanical damage on the $LiNbO_3$ surface, which is very undesirable. To prevent such damage on the surface, the etching time was carefully adjusted to leave a very thin layer of Ti film on the surface of etched samples and remove it afterward in a wet etching process.

The wet etching process was carried out using a diluted solution of hydrofluoric acid (HF) in De-Ionized (DI) water. Immersing the sample in a mixture of this solution with a ratio of HF : H_20 = 1 : 30 removed the thin Ti film and remnant residues from the

surface of the $LiNbO_3$ sample. Since this process is to basically clean up the very thin Ti layer and residues, it takes only a few seconds to perform. Thus, its time duration should be very carefully monitored. As the last step of the photo lithography process, stripping of the photoresist was carried out using AZ 300T photoresist stripper (from AZ Electronic Materials) to remove it from the top of the Ti stripe patterns. The photoresist stripper with the sample in it was heated to 90 ^{o}C and held for duration of 15 minutes at 90 ^{o}C temperature for its complete removal.

After the confirmation of the Ti film thickness by the Dektak surface profiler, the Ti stripe patterns were thermally diffused into the $LiNbO_3$ wafer (Appendix IV). The diffusion depth (d) is critical for controlling the optical properties of final channel waveguides. As expressed in previous research [28], and is evident form equations (89) and (90), diffusion temperature needs to be controlled more precisely than diffusion time.

$$d = 2\sqrt{Dt} \tag{89}$$

$$D = D_o e^{-\frac{Q_d}{k_o T}}. \tag{90}$$

Equation (90) is the expression for the diffusion coefficient (D) dependence on the bulk diffusivity D_o and the activation energy Q_d. D_o and T_o are material-dependent properties and for $LiNbO_3$ $D_o = 2.19\times10^{-4}$ cm^2/s, and $Q_d = 2.18$eV [29]. k_o is the Boltzmann constant, and 8.617×10^{-5} eV/K [22].

The patterned Ti stripes were diffused thermally into the $LiNbO_3$ in an open tube furnace. If the Ti is over-diffused, insertion loss of the waveguides increases, and multi-

mode waveguides may result. In this research, the $LiNbO_3$ wafer was placed at the center of a quartz tube, and the furnace temperature was set to 1125~1130 ^oC. The diffusion time varied between 11 to 15 hours and was performed under wet ambient condition. The diffusion temperature and the time were adjusted depending on the thickness of the Ti film. The wet ambient was introduced through a bubbler into the quartz tube to suppress the out-diffusion of Li_2O from the $LiNbO_3$ substrate [30].

After completion of the diffusion, both end edges of the waveguide were polished to ensure good coupling of light between a fiber and a waveguide (Appendix V). Three different grit sizes of a diamond pad were used for polishing. The pad with the largest grit size (15 μm) was used to grind out rough edges that result from the dicing process and also a remnant narrow Ti rim that forms from thick photoresist near the edges of the substrate during the lithography process. The other two pads (3 μm and 1 μm) were used subsequently in descending order of grit size to produce waveguide ends that are flat, smooth and shiny.

B. Aluminum Electrodes

Electro-optic devices are generally fabricated by delineating metal surface electrodes with a good electric conductivity onto or along channel waveguides. In this research, aluminum (Al) electrodes were patterned by the conventional lithography technique, in a similar fabrication process as of the Ti stripe patterns (Appendix VI). Also, the thin Al films were deposited utilizing the same sputtering system that was used

for the Ti deposition, which supports both DC magnetron and RF sputtering. Prior to the Al deposition, 160-nm-thick silicon dioxide (SiO_2) film was deposited on the clean surface of the channel waveguides as a buffer layer via RF sputtering. This prevents direct contact between the aluminum electrodes and the channel waveguides. The thickness of the SiO_2 film can be critical for the overall performance of final devices. If the SiO_2 buffer layer is too thin, mobile electric charges can interfere with the applied electric field, and degrade the desired electro-optic effect. On the other hand, if it is too thick, the overlap between the optical wave and the applied electric field becomes low and lead to higher electric voltage requirement for inducing electro-optic perturbations. After the deposition of the SiO_2 buffer layer, a thermal annealing of the SiO_2 film was conducted for 25 minutes at 900 ^oC with oxygen (O_2) flow of 100 sccm. This helps make the buffer layer denser, and can alleviate electric interference issues from mobile charges.

On the top of the annealed SiO_2 layer, the aluminum (Al) film was deposited by the AJA DC magnetron sputtering system. To fabricate the electrode patterns, the photo lithography process was performed with the same photo resist and the developer solutions as in the channel waveguide fabrication process. However, UV exposure time and developing time needed to be controlled more precisely because the surface of the Al film was shinier and more reflective than the surface of the Ti film. After the developing process is done, a thermal post curing in an oven at 135^oC for 15 minutes was also added to harden the photoresist (PR) patterns, so it can endure during wet etching process. Then, the wafer with PR patterns on it was cycled through an Al wet-

etching process to delineate the desired patterns. The sample was immersed into commercial aluminum etchant solution from J.T. Baker, and etched for approximately four minutes until the aluminum film was etched off, and the transparent surface of the $LiNbO_3$ was revealed.

CHAPTER V

MEASUREMENTS AND ANALYSIS

In this chapter, optical measurement results and analysis of those results are presented. First, the properties of the Ti channel waveguides are given. Next, the responses of the polarization converter and the phase shifter as obtained with an optical spectrum analyzer (OSA) or an optical vector analyzer (OVA) are reported. Then, the observed polarization control behavior from the OVA measurements are described in a Poincare sphere representation.

A. Ti Diffused $LiNbO_3$ Channel Waveguides

Ti diffused $LiNbO_3$ channel waveguides are the most fundamental part in integrated optical devices. They provide a pathway for optical waves to travel through. As such, the fabrication of optical channel waveguides requires accurate control for establishing the proper foundation for any final devices. In most cases, single mode optical waveguides are desirable for device operation. If a waveguide supports multiple modes, then optical modes interfere with each other and desired output properties of an optical guided wave, such as intensity, frequency and SOPs may be altered. In a polarization controller case for example, the phase-matched wavelength could be obscured, and the spectral output can be distorted. Other criteria for optical waveguides

include low insertion loss, and good confinement of the guided mode [31]. These criteria for channel waveguides should apply to both the TE and the TM polarizations.

Insertion loss measurements were carried out for each of the TE and the TM polarization modes using the amplified spontaneous emission (ASE) from an erbium-doped fiber (EDF) as a broad-band light source. Through a 980/1550 nm WDM coupler, the Erbium-doped fiber was pumped by a 980 nm laser diode (SDL Optics Inc. Model: SDLO-2400-090). The output of the coupler was connected with an optical isolator to prevent self-oscillation. The erbium doped fiber was spliced with a polarizing (PZ) fiber to enable selection of either the TE or the TM as an input polarization into the sample by an axial rotation of the PZ fiber. The launched polarization was controlled to obtain extinction ratios typically below -30 dB by simply rotating the PZ fiber, which leads to good suppression of the unwanted orthogonal polarization.

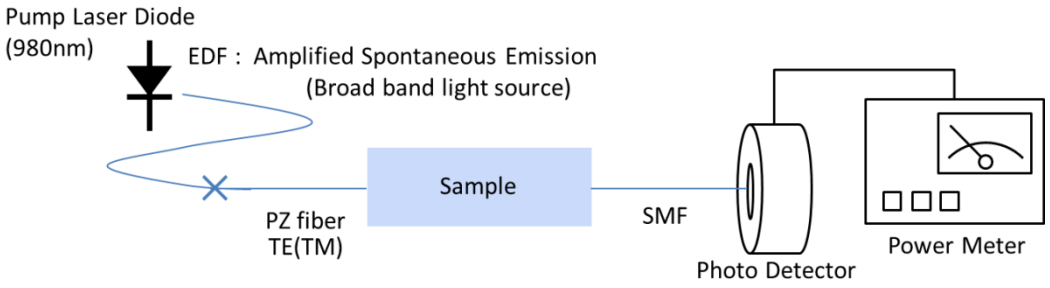

Fig. 10. The test setup for measuring the insertion loss.

Figure 10 shows the test setup for the optical insertion loss measurement. The input light from the PZ fiber was coupled to an edge of a channel waveguide by butt coupling. After traveling through a waveguide, the output light at the opposite edge was coupled into a single mode fiber (SMF). The emerging light out from the fiber was detected on a germanium photo detector (Newport, Model 818-IR), and the output power, P_{out}, was measured with a power meter (Newport, Model 1825-C). To optimize the output optical power, optical fibers and the device were placed on x-y-z translation stages to accurately manipulate the position of the sample and fibers.

From the measured optical power values, the insertion loss was calculated in dB using equation (91).

$$\textit{Insertion Loss (dB)} = -10\log\frac{P_{out}}{P_{in}} \tag{91}$$

P_{in} is the measured power through fiber-to-fiber without passing in a channel waveguide.

Table 2 The Parameters for Fabrication of Waveguide and Measured Insertion Loss Values.

Sample	Ti thickness (Å)	Diffusion Temperature (^{o}C)	Diffusion Time (hr)	Insertion Loss (dB)	
				TE	TM
PS13	910	1030	11	2.044	1.812
PS15	874	1030	9.5	1.897	1.686
PS25	929	1030	15	2.551	2.185

Single mode channel waveguides were fabricated by the thermal diffusion of the Ti film on x-cut y-propagating $LiNbO_3$ substrates as described in the device fabrication section. The desired thickness of Ti film ranged from 870 Å to 930 Å. The length of the edge-polished channel waveguide was 37 mm, and the channel width was 7μm. To optimize the quality of the waveguides, the effects of the various fabrication parameters such as diffusion temperature, diffusion time, and film thickness were investigated. Table 2 summarizes the diffusion parameters and measured insertion loss values of channel waveguides.

Single mode operation for both orthogonal polarizations was confirmed by examining the near field output mode profiles from the waveguides. A pig-tailed DFB laser diode (Alcatel, Module: 1915-LMI) with 1558 nm was used as a light source, and a current source (ILX Lightwave, Model: LDX-3207B) was used to drive the DFB laser diode. The fiber from the laser diode was spliced to a single mode fiber (SMF), and then connected to a fiber polarization controller (Thorlabs Inc., Model FDC010). The laser output light from the single mode fiber was launched into a channel waveguide by butt coupling. The light coming out of the channel waveguide was passed through an objective and focused onto BP109-IR optical beam profiler equipped with a germanium photo detector from Thorlabs Inc. The detector was equipped with an aperture with a diameter of 9 mm and a slit size of 5 μm. The detected optical wave was processed via Thorlabs analyzing software, and displayed on the monitor of a computer. The measurement setup for the mode profile is shown in figure 11.

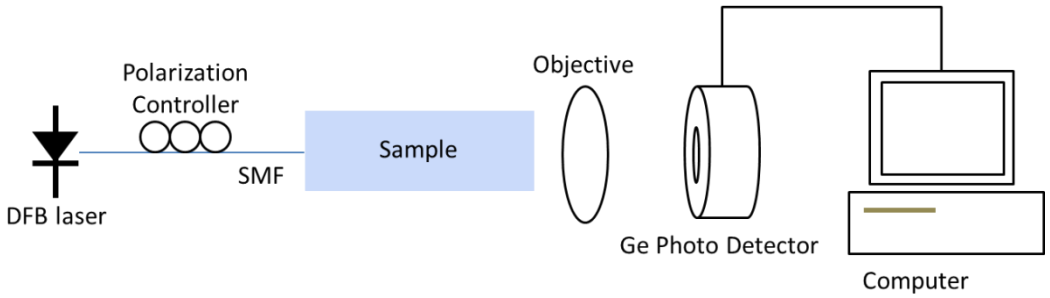

Fig. 11. The arrangement for the mode profile measurement.

As in the insertion loss measurement, x-y-z stages were used for the precise control of the position of the light on the mode profiler as well as a coupling between a fiber and a waveguide. Figure 12 shows 2-dimensional contour plots of the output intensity from the waveguide on sample PS13 for both TE and TM polarizations. Both contour plots for TE and TM polarization display only one optical mode. This can also be confirmed by profiling the output intensity.

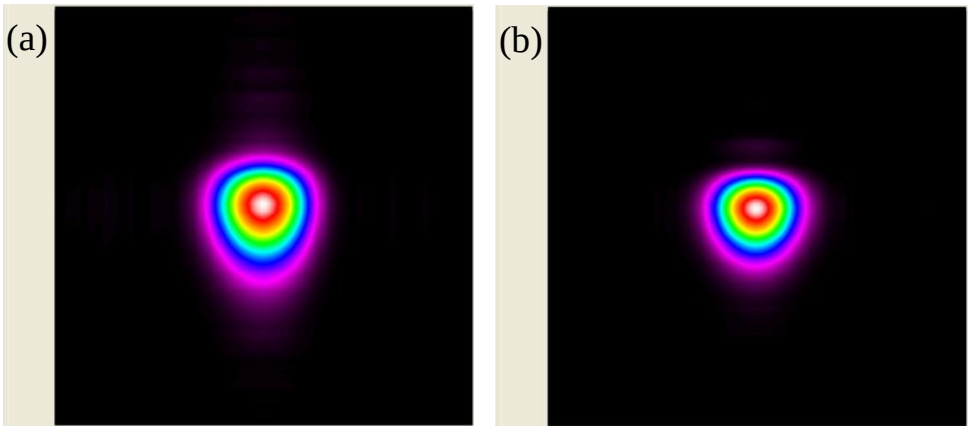

Fig. 12. 2-D contour plots of output intensity for (a) TE input polarization and (b) TM for PS13.

The intensity profiles corresponding to the 2-D contour plots of figure 12 are shown in figure 13 and 14. Figures 13 (a) and (b) show the horizontal and vertical intensity profiles for the TE polarization. As expected, the horizontal profile (figure 13-a) has a Gaussian distribution, which is symmetric, and the vertical intensity profile in figure 13 (b) shows an asymmetric Hermit-Gaussian distribution.

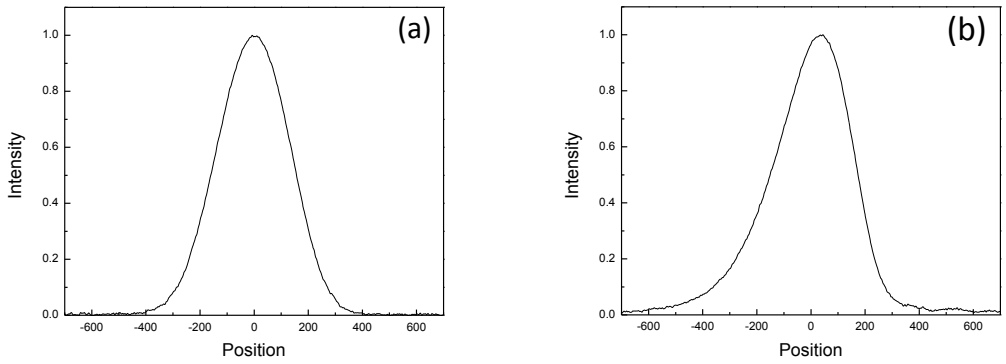

Fig. 13. The intensity profile of TE polarization out of the channel waveguide for (a) horizontal scan and (b) vertical scan.

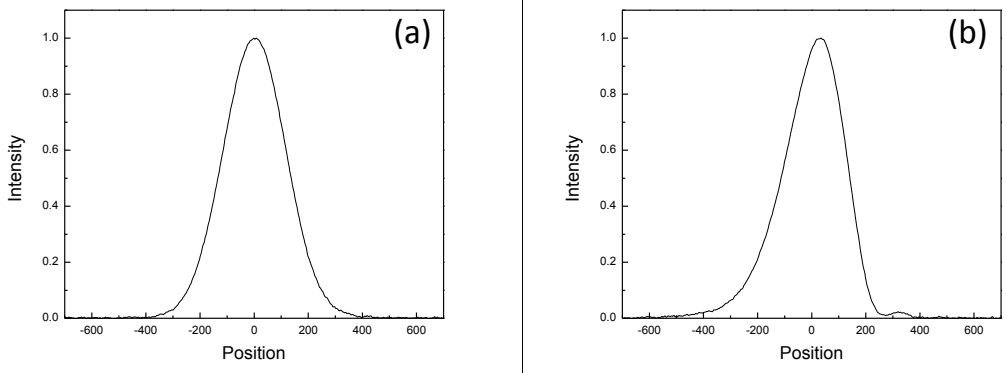

Fig. 14. The intensity profile of TM polarization out of the channel waveguide for (a) horizontal scan and (b) vertical scan.

Figure 14 (a) and (b) are the horizontal and vertical intensity profiles for the TM polarization corresponding to figure 12 (b). They also show similar distributions as of the TE case, Gaussian for the horizontal profile and Hermit-Gaussian for the vertical profile. Clearly, the intensity profiles shown in figure 13 and 14 match well with 2-D contour plots in figure 12, and confirm that the tested channel waveguide supports a single mode optical mode propagation for both TE and TM polarizations.

B. Polarization Converter and Phase Shifter

The polarization converter and the phase shifter are essential elements for producing a functional polarization controller. Each of these elements was characterized separately on the integrated device before evaluating the overall performance of the integrated device.

The broadband light source of erbium-doped fiber was used again for the evaluation of the polarization converter. The coupling of the light into a channel waveguide was identical to the insertion loss measurement method. The optical wave emerging from the channel waveguide was focused by a 20x objective, and passed into a polarization analyzer. Then, the optical beam was focused through another 20x objective, and coupled into a single mode fiber connected to the optical spectrum analyzer (OSA) (Anritsu, Model: MS-9710C), and the spectral intensity was monitored. The setup for the OSA spectral characterization is depicted in figure 15.

The intended thickness of the Al electrode film was 1100 Å. The polarization converter had the structure of inter-digitized electrodes, and the spatial period (Λ) of the electrode was 21 μm, which was designed based on equation (58) for the phase-matched wavelength of 1531 nm. The input polarization was controlled by the rotation of the polarizing fiber.

The overall device contained three electro-optic elements, and had four electrode pads including a common ground for connection to voltage sources. The electrode pads were wire-bonded by silver conductive paste, and voltages to the polarization controllers and the phase shifter were applied through operational amplifiers by utilizing a digital-analog-converter (DAC, model: AD-5379 from Analog Devices) that was controlled by a computer.

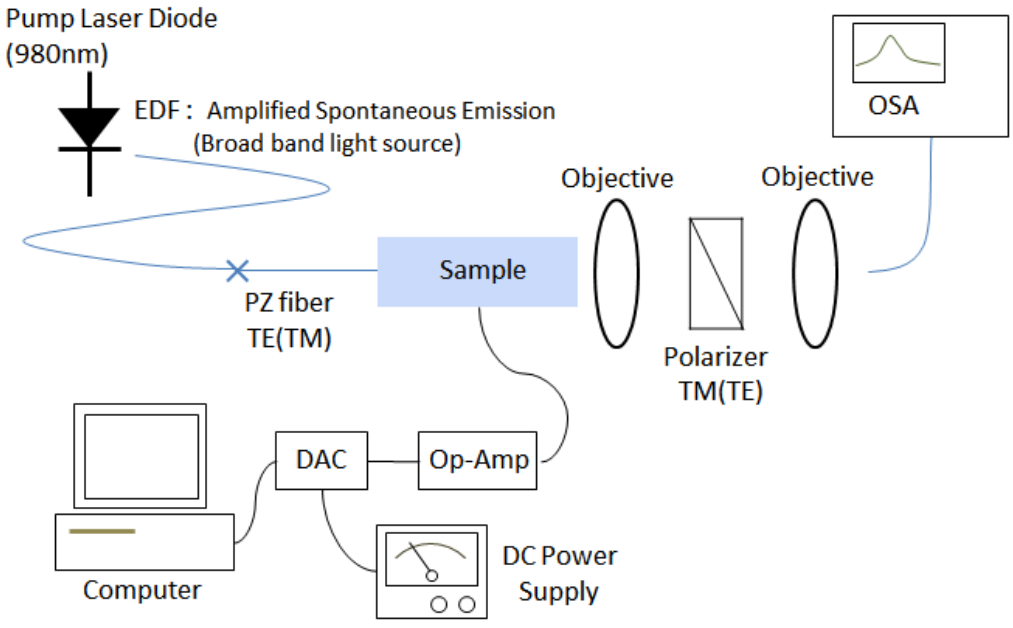

Fig. 15. The arrangement of OSA measurement with the ASE-EDF light source.

The device was placed on a flat copper plate connected to an x-y-z stage. Thermo-electric cooler/heater was attached under the copper plate, so the phase matched wavelength can be thermally tuned. Depending on the used Ti thickness and diffusion conditions during fabrication, the phase-matched wavelength can be slightly off the desired value even though the device was designed to function at near the peak emission intensity of the erbium-doped fiber light source (~ 1531 nm). Thus, samples were thermo-electrically heated or cooled to shift the phase matched wavelength close to the desired 1531 nm.

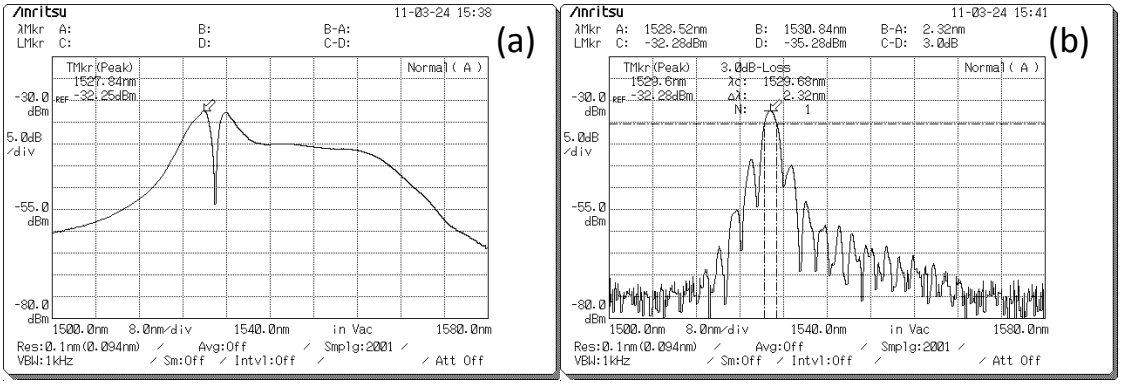

Fig. 16. Output spectra of a single converter on sample PS13 for TE input polarization with the analyzer set to pass (a) TE and (b) TM (sample temperature is 22.6 ^{o}C).

Figure 16 shows the converted and unconverted output spectra of the polarization converter on sample PS13 obtained by the OSA. A single converter configuration included on sample PS13 was tested first to confirm the operation. The spectra in figure 16 depict the responses for TE input polarization. Samples were thermo-electrically

heated or cooled to tune the phase matched wavelength to near the peak emission intensity of the erbium-doped fiber light source (~ 1531 nm). At 22.6 ^{o}C temperature setting maximum conversion on PS13 was achieved under an applied voltage of 19.89 V for TE mode and 20.03 V for TM mode. The measured 3-dB bandwidth values $\Delta\lambda_{3\text{-dB}}$ were 2.32 nm for both TE and TM input polarizations.

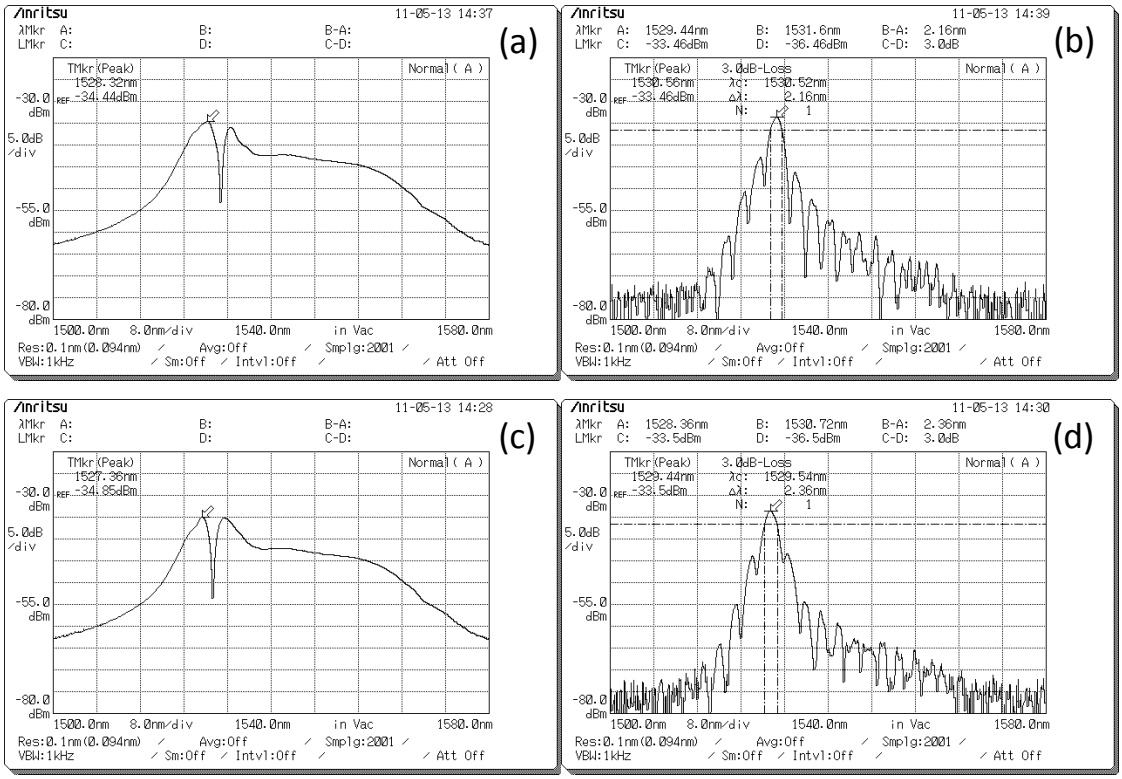

Fig. 17. Output spectra of the individual converters from a cascaded two-converters configuration on sample PS13 for TE input polarization: when V_{c1} = 17.2 V, V_{c2} = 0 V with the analyzer set to pass (a) TE and (b) TM; and when V_{c1} = 0 V, V_{c2} = 17.8 V with the analyzer set to pass (c) TE and (d) TM (sample temperature is 29.5 ^{o}C).

Once the single converter operation was confirmed, the configuration containing two converters in tandem along a single mode channel waveguide were next investigated. As described before, a digital-to-analog converter (DAC) followed by operational amplifiers was used to apply electric voltages to the electrodes. The computer controlling DAC provided the programmability of the electric field. Figure 17 shows the conversion result of each converter individually for the cascaded converters set on sample PS13. The sample was thermoelectrically heated to 29.5^{o}C. Generally, the polarization converters are supposed to function at the same phase-matched wavelength, but a slight offset is observed. The polarization conversion efficiency (PCE) for PS13 for the tested single converter was calculated using the OSA data files of the spectrum in figure 16 by using:

$$PCE = \frac{P_{conv}(\lambda)}{P_{conv}(\lambda) + P_{unconv}(\lambda)} \tag{92}$$

where $P_{conv}(\lambda)$ is the power of the converted polarization, and $P_{unconv}(\lambda)$ is the power of the unconverted polarization at the phase-matched wavelength λ. The calculated PCE form the OSA acquired data of the single polarization converter is 99.5 %, and the spectrum is well-matched with the expected theoretical response as well as shown in figure 18.

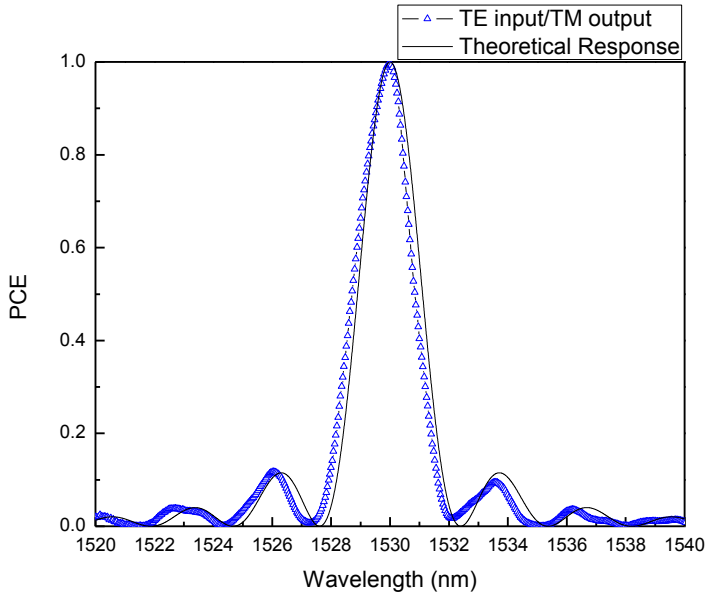

Fig. 18. The polarization conversion efficiency of the single polarization converter on sample PS13.

Although each converter in the two cascaded converters configuration displayed a good conversion property separately (figure 17), the phase-matched wavelengths were slightly different as stated earlier. This means that a deviation in birefringence for the guided light must clearly exist. As noted on the OSA spectra (figure 17), the phase-matched wavelength of the first converter and the second converter are 1530.56 nm and 1529.44 nm, respectively. Ideally, if there is no difference in the birefringence of the individual converters, the second converter should be able to rotate the converted output from the first converter back to the original input polarization. However, the second converter was unable to switch the polarization of the output from the first converter

back to the original input polarization due to the birefringence variation in each converter, and possibly perturbation of the retardation through the optical path length between the two converters as displayed in figure 19. From figure 19 (a), it can be observed that although for TE input the converted output of the first converter is well suppressed, the output polarization in the cascaded configuration test is not fully restored back to the original incident polarization by virtue of the second peak appearing in figure 19 (b).

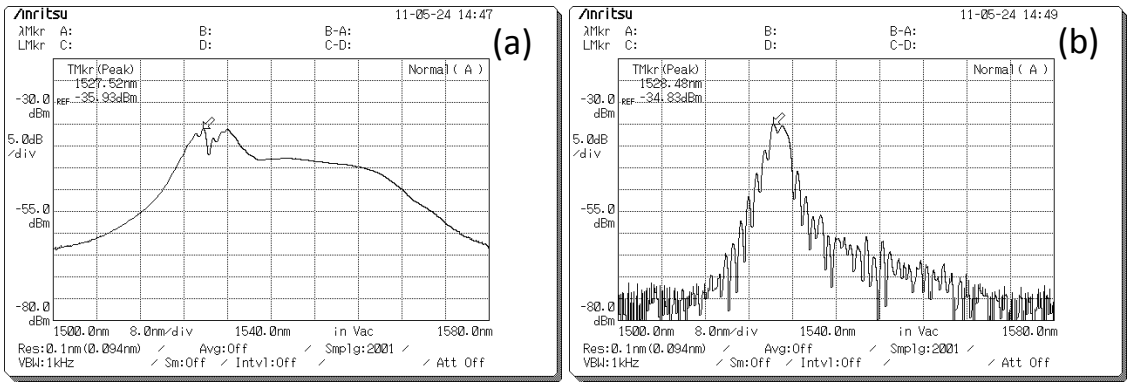

Fig. 19. The output spectra of the cascaded polarization converters for TE input with 90^{o} rotation through each converter for (a) TE output and (b) TM output on sample PS13.

There could be several reasons for this behavior. The most probable are non-uniformity of the Ti film thickness, the presence of a temperature gradient along the quartz tube during the diffusion process, and also slight deviations from the desired separation length between the cascaded converters caused during fabrication.

The phase shifter formed with two parallel electrodes along the channel waveguide was also produced during the converters electrode fabrication step. The length of the electrodes set is 6,000 μm. The phase shifter was tested at room temperature with an optical vector analyzer (OVA) from LUNA Innovations Inc. The OVA can provide the relative phase delay between the two orthogonal polarization components at the output. When an electric voltage is applied on the phase shifter along the z-direction, which is the direction normal to the wave-propagation, the electric field across two electrodes can be estimated by dividing the applied phase shifter voltage (V_s) by the gap (g) between electrodes. However, in the actual device the electric field does not fully interact with the optical field, and an overlap factor (α) should be included. Thus, equation (67) becomes

$$\delta\phi = \frac{\pi}{\lambda_o}\left[\left(n_{TE}^3\gamma_{33} - n_o^3\gamma_{13}\right)\frac{V_s}{g}\alpha\right]\ell . \tag{93}$$

Figure 20 indicates that the required applied voltage for inducing a phase shift of π radians, V_π, near 1529.4 nm wavelength is 40 V. This means that constructive interference can be turned into destructive interference by applying a voltage of 40 V, and vice-versa. For an ideal overlap ($\alpha = 1$) the calculated V_π from equation (93) is 16.4 V. Comparing to the measured value, the overlap factor for the phase shifter is estimated to be 0.41.

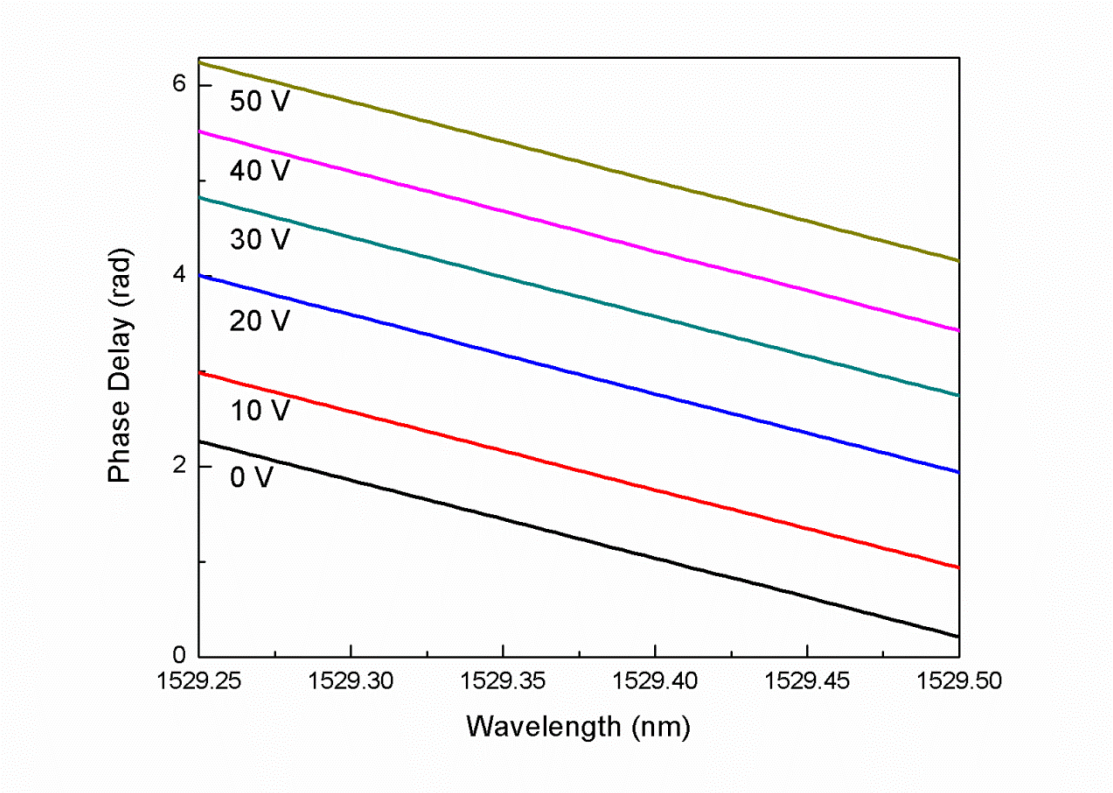

Fig. 20. The electro-optically induced phase delay (rad) by the phase shifter based on the applied voltages for PS25.

C. Polarization Control

Following the characterization of the thermally tuned individual elements on sample PS13, the overall integrated device consisting of the two polarization converters with a phase shifter between them was evaluated for its polarization control property. The tests were performed for an integrated device configuration on sample PS25 by utilizing an optical vector analyzer system (OVA) and carried out at room temperature due to the lack of sample temperature control on the OVA setup. The OVA system

utilizes polarization-diverse swept wavelength interferometry, and enables the measurement of the output optical field magnitude and phase response [32, 33]. However, the measurement data include not only the behavior of a device under test (DUT) but also the influence of the optical fiber as well. Recently, research at Texas A&M by Kim et al. [34] developed an algorithm to extract the behavior of the DUT from the measured data.

In this work, the raw data from the OVA was processed using Kim's algorithm and analyzed. In what follows, the measured optical spectra from the OVA are compared to simulated plots based on the coupled mode theory. In addition, the results are also described in a Poincare sphere representation for the phase-matched wavelength.

In the initial measurement stage, the separated pair of polarization couplers was tested as a combined set for complete TE↔TM conversion in a two-step additive polarization coupling process. Since complete conversion between orthogonal modes requires 90^o rotation between the input and output states of polarization, each converter may be set to induce a rotation of 45^o electro-optically. For this to occur, the birefringence in the waveguide should remain constant, hence the phase-matched wavelength of the two converters would be the same, and the phase delay for propagation between the two converters must be $m(2\pi)$ with m an integer.

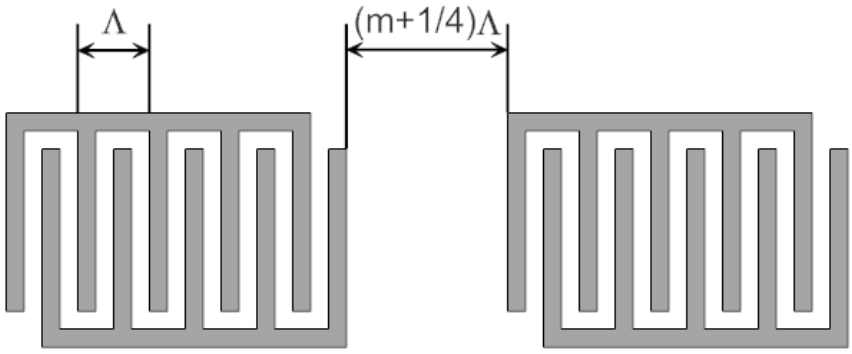

Fig. 21. The separation between the two polarization converters used in the electrode design.

By taking the periodicity of the converters at the phase matched wavelength into account, the separation length between the two polarization converters was designed to be (m+1/4)Λ as shown in figure 21. This would allow for the rotations from the individual converters to add up as if it is a single continuous converter, while providing a spatial region for the insertion of the phase shifter. A simulation was performed to validate this principle. The simulated plot in figure 22 confirmed that the output spectrum for the two cascaded converter sets with a separation of Λ/4 (for m=0) is identical to a single continuous polarization converter with a doubled coupling length relative to the coupling length of the individual converters in the cascaded configuration.

However, as seen in figure 23, when each converter on sample PS25 was tested at room temperature separately, the phase-matched wavelength of the two converters did not coincide. The dip for the TE input from the first converter is at 1527.36 nm, while the dip from the second converter is at 1529.76 nm. Thus, an offset of 2.4 nm for the

phase-matched wavelength existed between the two converters for the integrated configuration on sample PS25. Since the measurement required a 45^o rotation through each converter for complete TE↔TM conversion between input and output, and because a 45^o rotation is equivalent to splitting the intensity of an incident (TE or TM) polarization equally between the orthogonal TE and TM polarizations, it was anticipated that the wavelength corresponding to the 3-dB drop in intensity (on the longer λ side) of the first converter would strongly influence the wavelength for maximum conversion at the output of the overall device, and should fall within the 2.4 nm offset of the phase matched wavelengths.

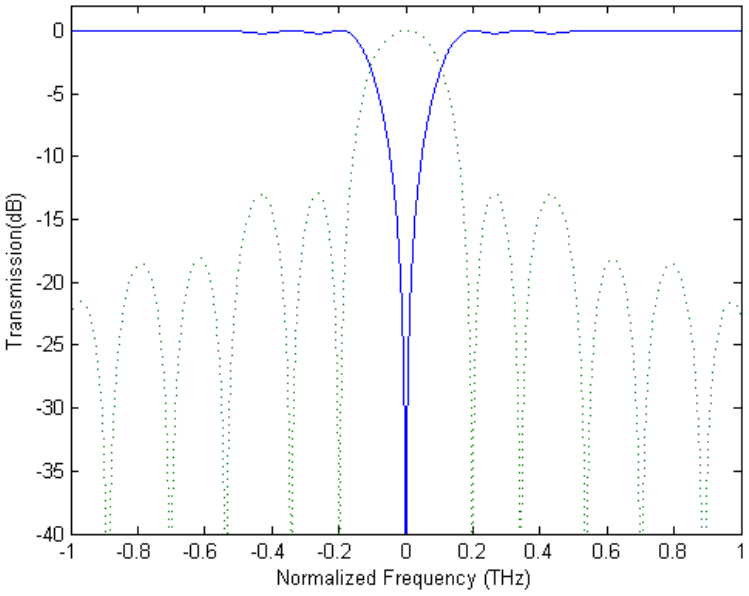

Fig. 22. Simulated polarization conversion for a cascaded converter configuration having a separation length of (m+1/4)Λ between them, with m = 0.

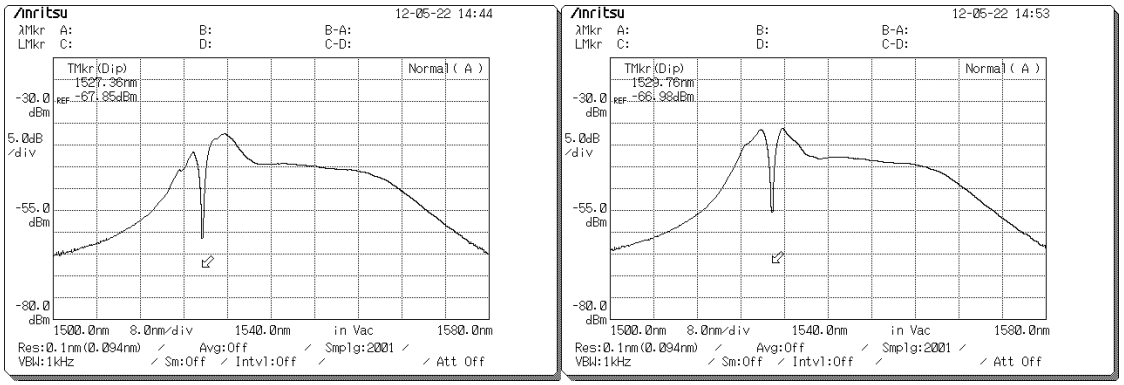

Fig. 23. Output spectra of the individual conversion a cascaded two-converters configuration on sample PS25 at room temperature for TE incident polarization, (a) V_{c1} = 22 V, V_{c2} = 0, and (b) V_{c1} = 0, V_{c2} = 20 V. For both V_P = 0 and the analyzer is set to pass TM polarization.

Figure 24 shows the output TE and TM spectral intensity for TE input polarization into the device. The applied voltage on the first converter was 16 V, and on the second converter was 14 V. The phase-matched wavelength is at 1529.42 nm, and the unwanted TE polarization shows a drop of approximately 40 dB. The zero voltage for the phase shifter indicates no significant additional phase delay is introduced at this wavelength through the separation length between the two converters. Furthermore, the observed maximum conversion at 1529.42 nm wavelength corresponds to the 3-dB drop in intensity (on the longer λ side) of the tested first converter obtained from the data files of figure 23, and it is indeed within the 2.4 nm offset of the phase-matched wavelength values of the individually tested converters (figure 23). A Poincare sphere representation for the evolution of this polarization conversion is shown in figure 25. The small red

circle represents the SOP at the output when an incident TE-polarized optical wave traversed the entire length of the sample without any applied voltages on the electrodes (i.e.; without experiencing any voltage induced perturbations). The small blue circle is the output SOP under the above stated voltages (V_{c1} = 16 V, V_{c2} = 14 V) for conversion from TE input to TM output. These two points were extracted from the OVA measurement data files at the observed 1529.42 nm wavelength for maximum conversion. The solid line between the two represents the pathway for the simulated SOP that an incident TE-polarized optical wave would experience through the device during conversion form a TE input to a TM output. The horizontal segment was obtained by increasing V_{c1} from zero to 16 V, in increments of ΔV= 1 V with V_{c2} = 0, and the vertical segment was obtained by varying V_{c2} from 0 to 14 V in increments of ΔV= 0.1 V while V_{c1} was maintained at 16 V. The disparity between the red circle and the starting point of the horizontal segment of the traced path in figure 25 is likely caused from imperfections during the fabrication processes, particularly misalignment with the y-axis of the crystal either during dicing or the waveguide photolithography patterning step. Other reasons for this error include ambient temperature induced variation of indices, as well as variations of the incident SOP induced from mechanical stress on the optical fiber.

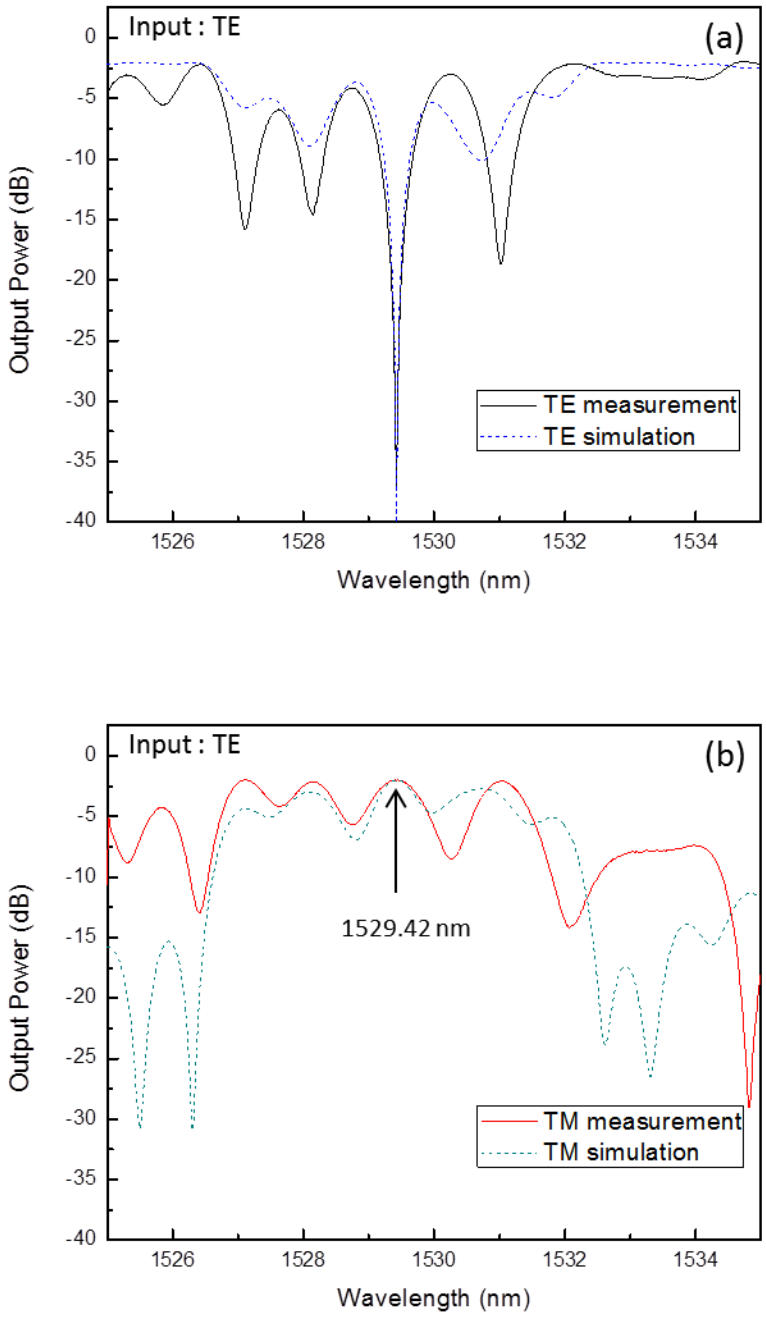

Fig. 24. Output spectra for the polarization conversion from incident TE to TM for (a) the TE output and (b) the TM output.

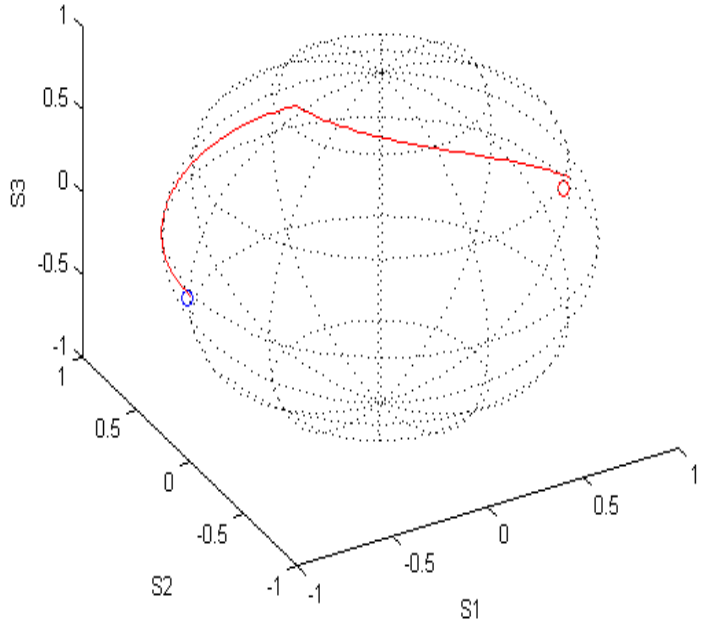

Fig. 25. Poincare sphere representation for transformation of the output from TE to TM of TE input. Red circle is TE output without applied voltages (no conversion), blue circle is TM output with applied voltages for 45^{o} rotation through each converter.

To investigate the effect of the phase shifter on the state of polarization at the device output, the voltage on the phase shifter was increased from 0 V to 50 V in increments of 5 V without changing the voltages that were applied on the converters. Figure 26 is the Poincare sphere representation for the output field vector obtained from the processed data acquired by the OVA. It indicates the transformation of TM output back to TE polarization when the applied voltage on the phase shifter was 40 V. This

confirms an induced π-radian retardation as was demonstrated in figure 20 with a 40 V on the phase shifter.

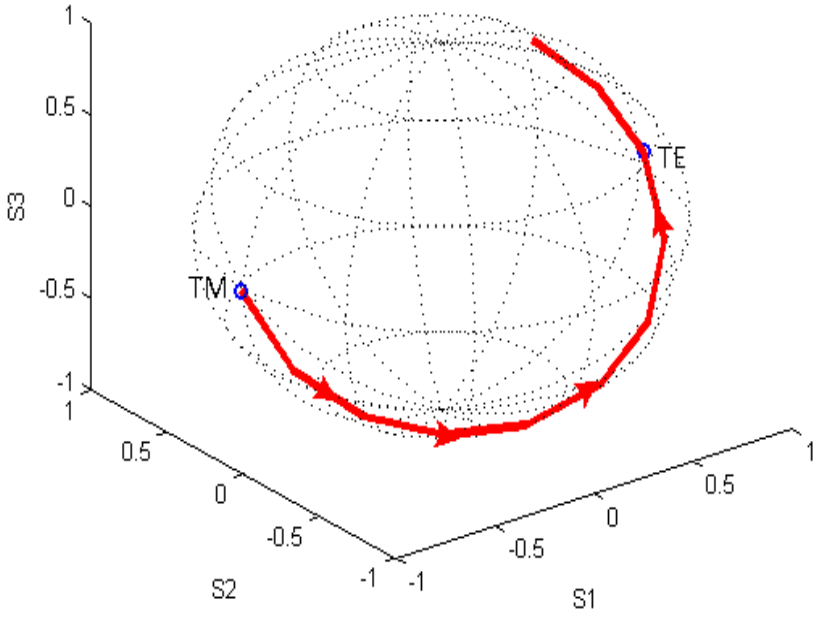

Fig. 26. The phase shift on the Poincare sphere.

Next the integrated device performance for TM incident polarization was investigated. Conversion to TE output polarization was achieved by 45^{o} rotation through each converter under the same voltage conditions (V_{c1} = 16V, V_{c2} = 14V, V_P = 0), and at the same wavelength λ = 1529.45 nm. Figure 27 shows the measured output TM and TE spectral intensity. Once again, a drop of approximately 40 dB was achieved for the unwanted polarization, which in this case is TM.

In addition to the TE and the TM input polarization cases, the device behavior for converting arbitrary incident polarizations to either TE or TM polarization at the output was also investigated. Experimental measurements and simulations were carried out for incident polarization angles of 45^o and 56^o, both relative to the z-axis of the crystal. Figures 28 and 29 show the obtained results for the TE and TM output polarization cases, respectively, from the 45^o incident polarization. In each case, the suppression for the unwanted polarization is nearly 40 dB at λ = 1529.45 nm. Poincare sphere representation for the 45^o incident polarization transformation to TM and TE output polarization are depicted in figure 30 (a) and (b), respectively. Experimental results of the output spectra from incident polarization at 56^o relative to the z-axis of the crystal for transformation to TM output are shown in figure 31, and in figure 32 for transformation to TE output, in both cases again near λ = 1529.41 nm. Poincare sphere representations for the evolution of the TE and TM outputs from an incident polarization at 56^o are shown in figure 33 (a) and (b), respectively.

Table 3 lists values for the incident polarization angle, the targeted output polarization state (TE or TM), and the applied voltages on each converter as well as the phase shifter for achieving the desired output polarization, all near λ = 1529.4 nm. The slight variations in the wavelength are attributed to variation in the ambient temperature during the testing for optical characterization.

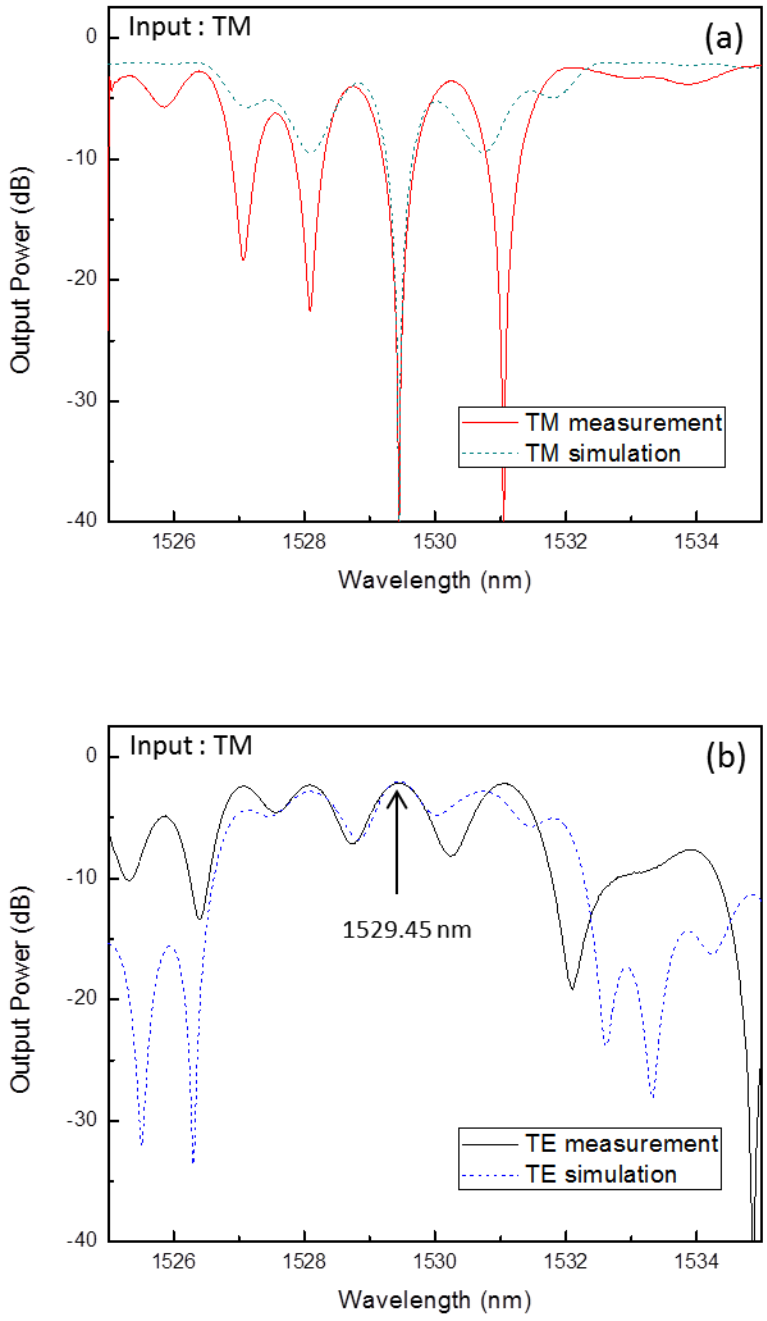

Fig. 27. Output spectra for the polarization conversion from incident TM to TE for (a) the TM output and (b) the TE output.

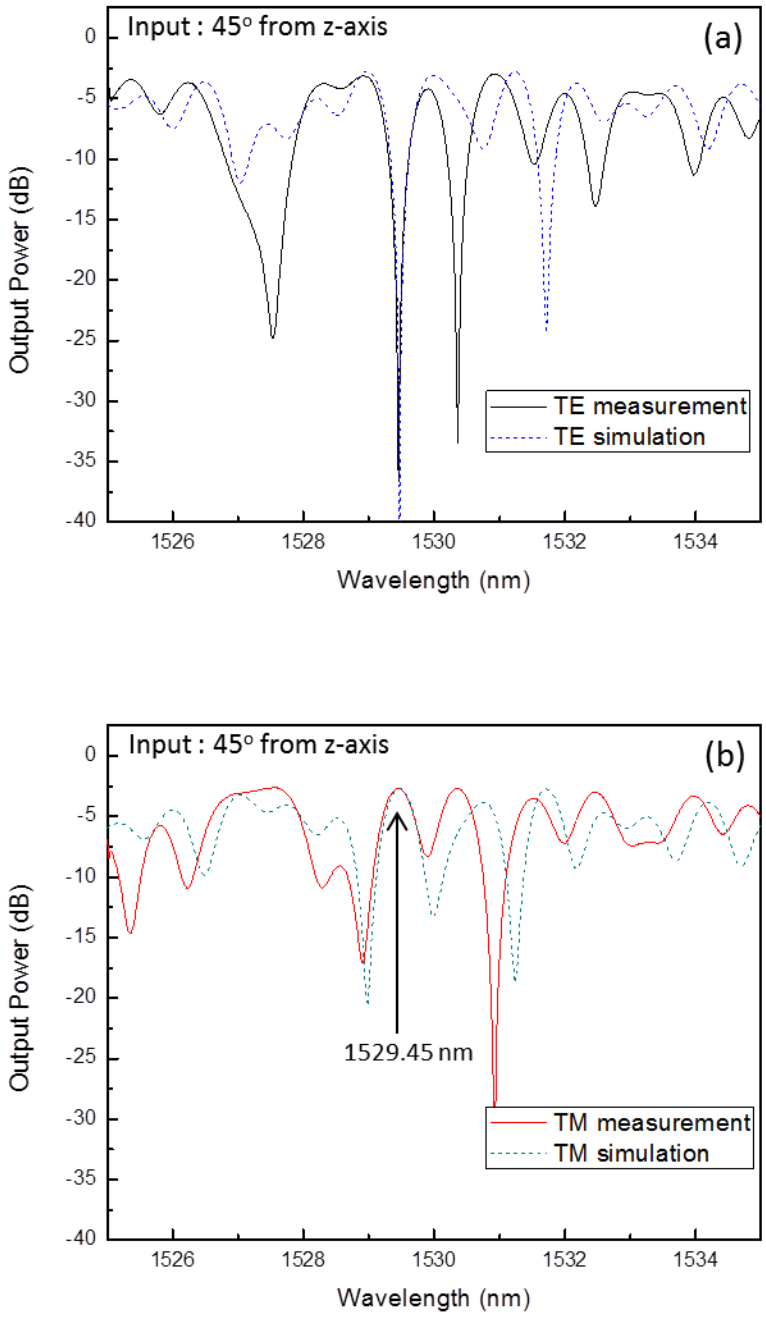

Fig. 28. Output spectra for the transformation from incident polarization at 45° relative to z-axis to TM polarization for (a) the TE output and (b) the TM output.

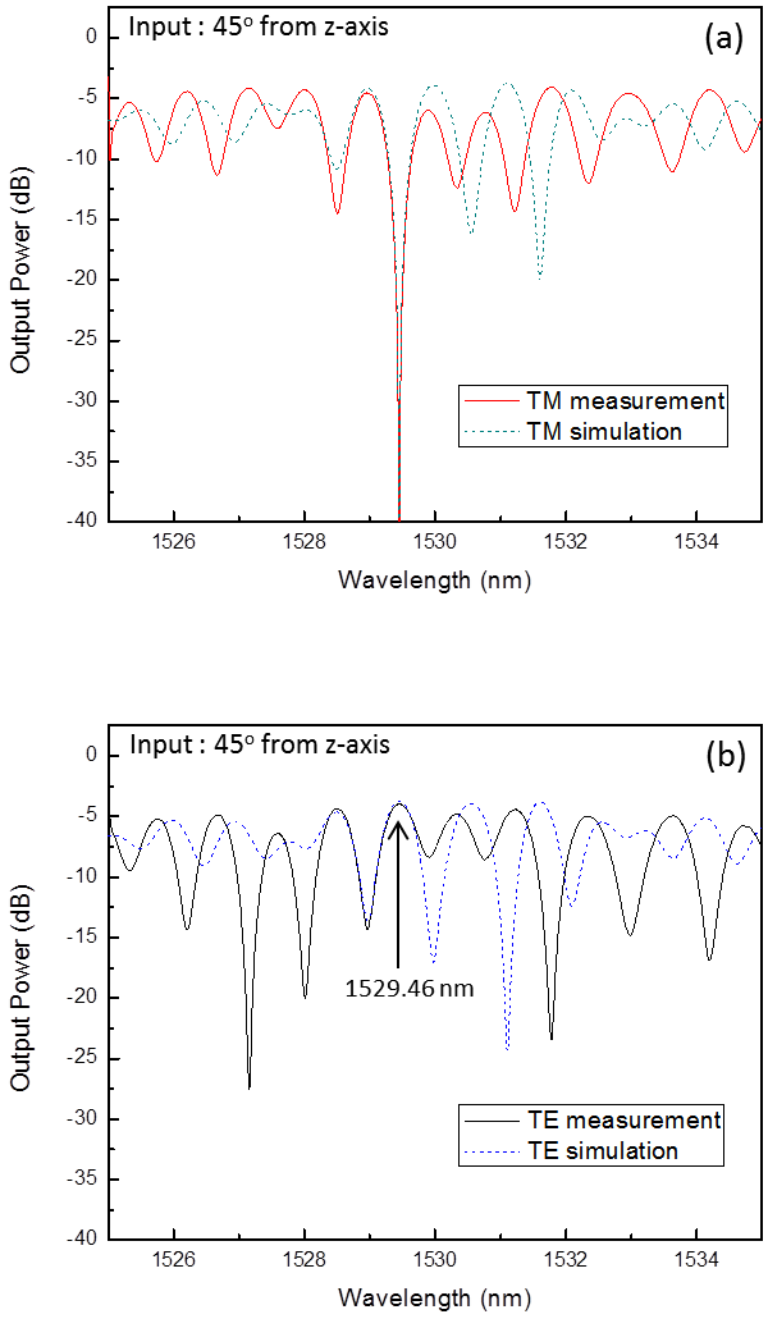

Fig. 29. Output spectra for the transformation from incident polarization at 45° relative to z-axis to TE polarization for (a) the TM output and (b) the TE output.

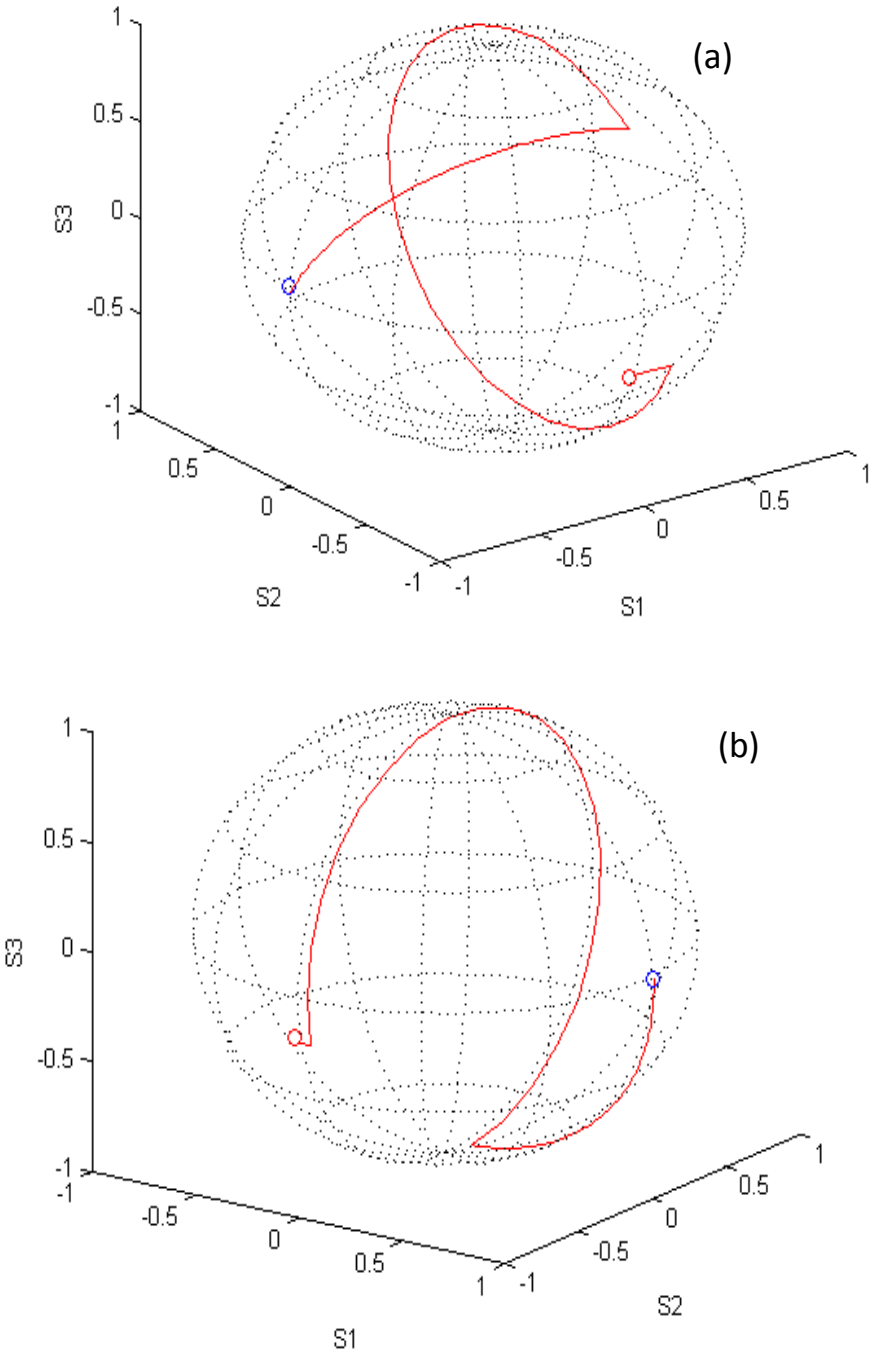

Fig. 30. The Poincare sphere presentation for the input of 45^{o} from x-axis to (a) TM and (b) TE output.

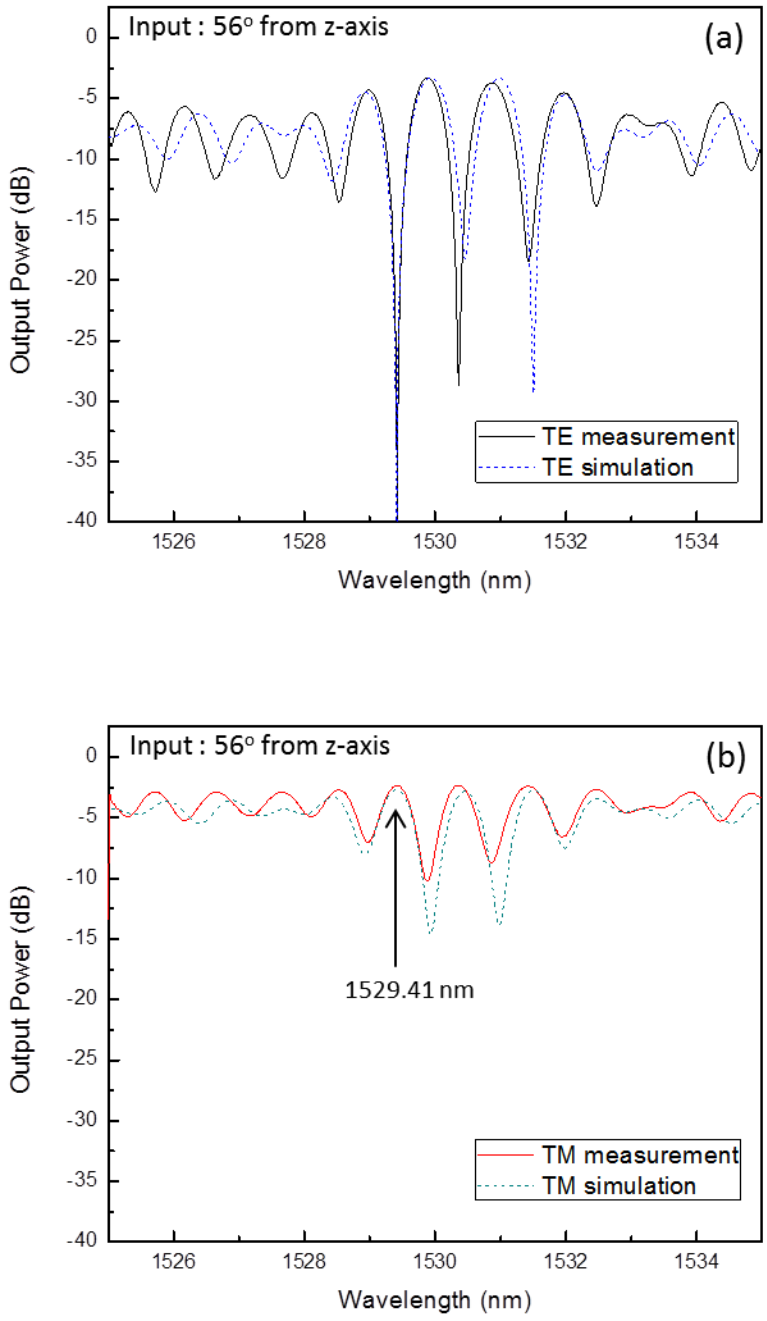

Fig. 31. Output spectra of the polarization transformation from incident polarization at 56^{o} relative to z-axis to TM polarization for (a) the TE output and (b) the TM output.

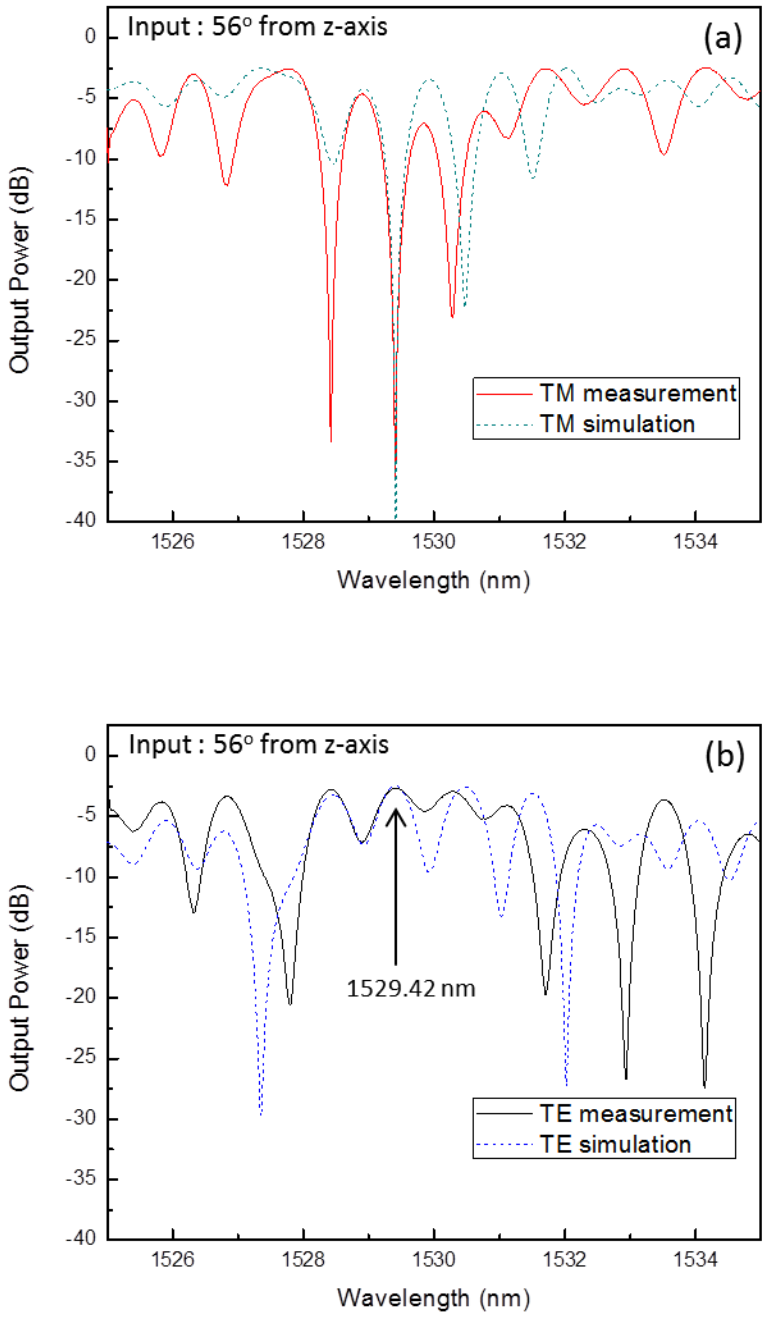

Fig. 32. Output spectra of the polarization transformation from incident polarization at 56^{o} relative to z-axis to TE polarization for (a) the TE output and (b) the TM output.

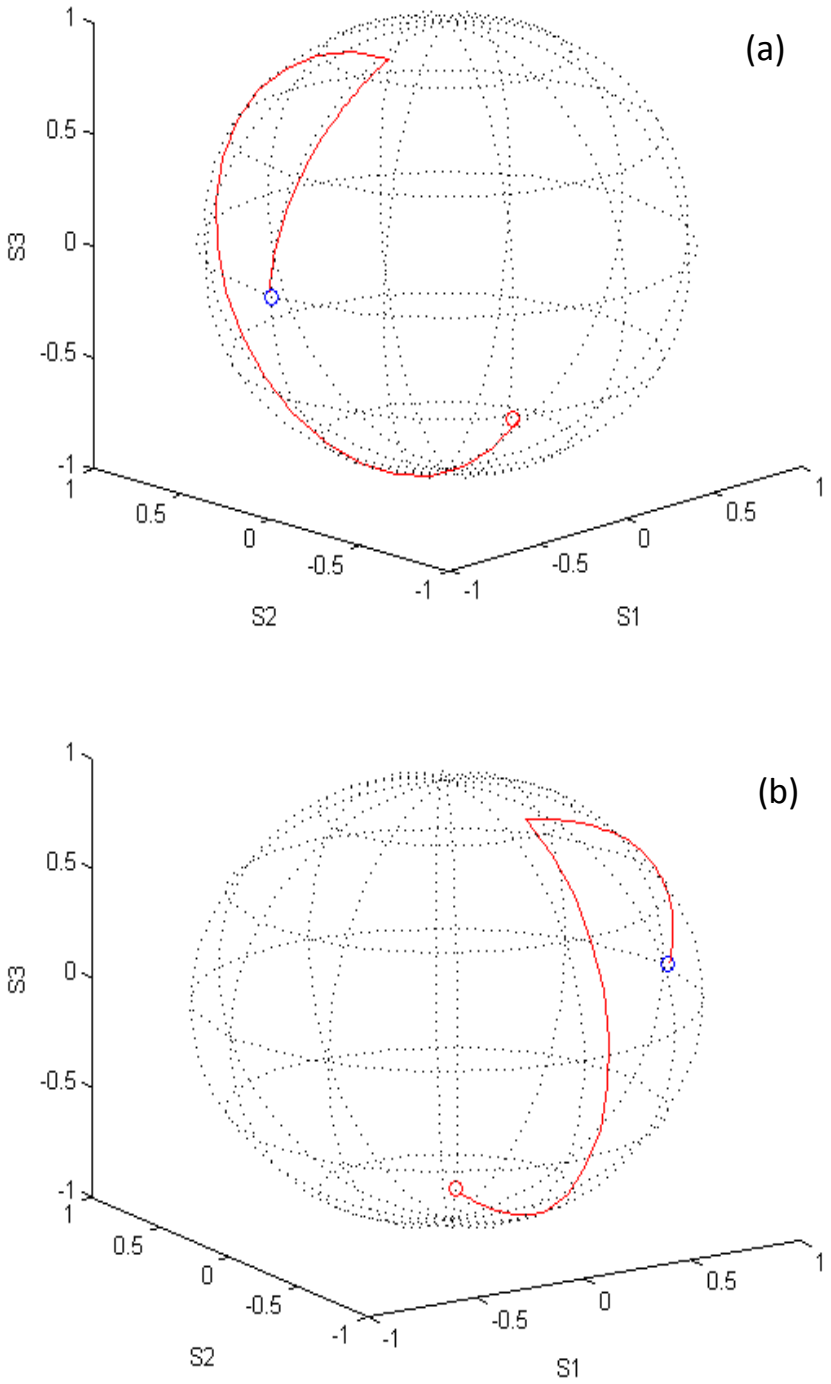

Fig. 33. The Poincare sphere presentation for the input of 56^{o} from x-axis to (a) TM and (b) TE output.

Table 3 The Parameters for Individual Polarization Control Measurements

Input	Output	Maximum Conversion Wavelength (nm)	Applied Voltage (V)		
			Converter 1	Phase shifter	Converter 2
0^o (TE)	TM	1529.42	16	0	14
90^o (TM)	TE	1529.45	16	0	14
45^o	TE	1529.45	3	10	16
	TM	1529.46	10	-5	8
56^o	TE	1529.41	10	45	-15
	TM	1529.42	0	-17	8

CHAPTER VI

CONCLUSION

A polarization controller utilizing the concept of two couplers and one retarder has been demonstrated via electro-optic effects. The device was fabricated on $LiNbO_3$ substrate, and designed to operate in the vicinity of the peak emission wavelength of the erbium-doped fiber amplifier. Although the concept of operation with two couplers and a retarder using bulk or fiber optic devices has been suggested before, and demonstrated with an electro-optic retarder in conjunction with other bulk components, this is the first demonstration for its operation of through electro-optic effects for the three elements combined. To emulate the bulk components approach, a device configuration composed of two polarization converters with a phase shifter centered between them, and all integrated on a single channel waveguide was used. The performance of the device is strongly dependent on the properties of the polarization converters as couplers and the phase shifter as a phase retarder.

Ti diffused channel waveguides were fabricated on an x-cut y-propagating $LiNbO_3$ substrate. The polarization converters and phase shifter were formed by patterning aluminum surface electrodes on top of a SiO_2 buffer layer. The polarization converters were produced in an interdigitated electrode form with a spatial period of 21 μm, over 10.5 mm coupling length. The phase shifter was implemented in the form of a 6,000 μm long electrode with 17 μm gap. The performance of the polarization converters is highly sensitive to the properties of the fabricated Ti diffused channel

waveguides. Fabrication parameters for the waveguides were optimized to produce polarization coupling at a phase-matched wavelength near 1530 nm with the used electrode arrangement. Single mode channel waveguides for both the TE and TM polarization were fabricated by diffusing 7- μm wide, 1030-Å thick Ti stripes at 1030 ^{o}C for a time duration of 15 hr. Single mode propagation was confirmed with a mode profiler. The polarization conversion performance of a single element on the sample was characterized with an optical spectrum analyzer, and it showed a maximum conversion efficiency of 99.5 % at 1529.6 nm wavelength. However, the phase-matched wavelength for two cascaded converters on the same sample revealed a 2.4 nm offset between them when they were tested individually. This was believed to be due to non-uniformity of the Ti film thickness or the furnace temperature along the quartz tube which ultimately affects the birefringence in the waveguide. The phase shifter was tested with an optical vector analyzer (OVA), from which the relative phase between the TE and the TM polarizations of the output optical wave was determined. The OVA also established the required voltage on the phase shifter for a π-radian phase shift to be 40 V.

The polarization transformation behavior for the overall integrated device configuration was also characterized with the OVA. Transformation of orthogonal or arbitrary incident polarizations to either TE or TM polarization at the output was investigated. Suppression for the unwanted polarization at the output of approximately -40 dB near 1529.4 nm wavelength was obtained with voltages on both converters for TE↔TM transformation, as well as 45^{o} and 56^{o} incident polarization. For the incident

orthogonal polarization case the transformation was realized without a voltage on the phase shifter supporting the implemented design parameters, and transformation of the obtained output back to its incident polarization through an induced π-radian retardation was confirmed by applying 40 V on the phase shifter.

To verify the functionality of the integrated device for potential dynamic polarization control applications, simulations for Poincare sphere representation for all the tested incident conditions were carried out and presented.

An extension of this research for enhancing the device response to arbitrary incident polarizations may be realized by inserting an additional phase shifter in front of the first polarization converter. This would provide a means to offset intrinsic phase retardation between TE and TM components which results from the birefringence of the substrate material. Furthermore, this could also simplify the required adjustments of voltages on the polarization converters for achieving either TE or TM outputs. For transformation to any other output polarization, the addition of another phase shifter after the second converter would provide a control for adjusting the phase between orthogonal components at the output. More importantly, an added phase shifter at the output would provide a scheme to control the phase between successive cells in an integrated configuration of multiple such unit cells.

REFERENCES

[1] C. Cole, I. Lyubomirsky, A. Ghiasi, and V. Telang, "Higher-order modulation for client optics," *Communications Magazine, IEEE,* vol. 51, pp. 50-57, Mar. 2013.

[2] E. Lach and W. Idler, "Modulation formats for 100G and beyond," *Optical Fiber Technology,* vol. 17, pp. 377-386, Aug. 2011.

[3] K. Roberts, D. Beckett, D. Boertjes, J. Berthold, and C. Laperle, "100G and beyond with digital coherent signal processing," *Communications Magazine, IEEE,* vol. 48, pp. 62-69, Jul. 2010.

[4] H. Takara, T. Goh, K. Shibahara, K. Yonenaga, S. Kawai, and M. Jinno, "Experimental demonstration of 400 Gb/s multi-flow, multi-rate, multi-reach optical transmitter for efficient elastic spectral routing," *European Conference on Optical Communications*, pp. Tu.5.A.4, Geneva, Switzerland, 2011.

[5] A. Leinse, M. B. J. Diemeer, A. Rousseau, and A. Driessen, "A novel high-speed polymeric EO Modulator based on a combination of a microring resonator and an MZI," *IEEE Photonics Technology Letters,* vol. 17, pp. 2074-2076, Oct. 2005.

[6] T. H. Wood, C. A. Burrus, D. A. B. Miller, D. S. Chemla, T. C. Damen, A. C. Gossard, *et al.*, "High-speed optical modulation with GaAs/GaAlAs quantum wells in a p-i-n diode structure," *Applied Physics Letters,* vol. 44, pp. 16-18, Jan. 1984.

[7] J. E. Toney, V. E. Stenger, J. Busch, P. Pontius, M. Clabough, A. Pollick, *et al.*, "Quasi-phase-matched electro-optic modulators for high-speed signal

processing," *Proceedings of SPIE*, vol. 8647, pp. 86470H-86470H-7, San Francisco, California, 2013

[8] J. M. H. Elmirghani and H. T. Mouftah, "All-optical wavelength conversion: technologies and applications in DWDM networks," *IEEE Communications Magazine,* vol. 38, pp. 86-92, Mar. 2000.

[9] J. M. H. Elmirghani and H. T. Mouftah, "Technologies and architectures for scalable dynamic dense WDM networks," *IEEE Communications Magazine,* vol. 38, pp. 58-66, Feb. 2000.

[10] M. E. Solmaz, D. B. Adams, W. C. Tan, W. T. Snider, and C. K. Madsen, "Vertically integrated As_2S_3 ring resonator on $LiNbO_3$," *Optics Letters,* vol. 34, pp. 1735-1737, Jun. 2009.

[11] M. Martinelli, P. Martelli, and S. M. Pietralunga, "Polarization stabilization in optical communications systems," *Journal of Lightwave Technology,* vol. 24, pp. 4172-4183, Nov. 2006.

[12] R. Noe, T. Pfau, M. El-Darawy, and S. Hoffmann, "Electronic polarization control algorithms for coherent optical transmission," *IEEE Journal of Selected Topics in Quantum Electronics,* vol. 16, pp. 1193-1200, Sep. 2010.

[13] H. Shimizu and K. Kaede, "Endless polarisation controller using electro-optic waveplates," *Electronics Letters,* vol. 24, pp. 412-413, Mar. 1988.

[14] R. Noe, H. Heidrich, and D. Hoffmann, "Endless polarization control systems for coherent optics," *Journal of Lightwave Technology,* vol. 6, pp. 1199-1208, Jol. 1988.

[15] F. Heismann, "Integrated-optic polarization transformer for reset-free endless polarization control," *IEEE Journal of Quantum Electronics,* vol. 25, pp. 1898-1906, Aug. 1989.

[16] F. Heismann, M. D. Divino, and L. L. Buhl, "Integrated-optic polarization controller with unlimited transformation range," *Applied Physics Letters,* vol. 57, pp. 855-857, Aug. 1990.

[17] L. Moller, "WDM polarization controller in PLC technology," *IEEE Photonics Technology Letters,* vol. 13, pp. 585-587, Jun. 2001.

[18] M. Martinelli and R. A. Chipman, "Endless polarization control algorithm using adjustable linear retarders with fixed axes," *Journal of Lightwave Technology,* vol. 21, pp. 2089-2096, Sep. 2003.

[19] P. Oswald and C. K. Madsen, "Deterministic analysis of endless tuning of polarization controllers," *Journal of Lightwave Technology,* vol. 24, p. 2932, Jul. 2006.

[20] B. Koch, R. Noe, V. Mirvoda, and D. Sandel, "Temperature-insensitive and two-sided endless polarization control," *IEEE Photonics Technology Letters,* vol. 24, pp. 2077-2079, Nov. 2012.

[21] C. A. Balanis, *Advanced engineering electromagnetics*, Wiley, New York, 1989.

[22] J.-M. Liu, *Photonic devices,* Cambridge University Press, Cambridge UK, 2005.

[23] A. Yariv and P. Yeh, *Photonics: Optical Electronics in Modern Communications*, 6th edition, Oxford University Press, New York, 2007.

[24] R. C. Alferness, "Efficient waveguide electro-optic TE↔TM mode converter/wavelength filter," *Applied Physics Letters,* vol. 36, pp. 513-515, Apr. 1980.

[25] J. H. Kim, "Novel birefringent frequency discriminator for microwave photonic links," Ph.D. Dissertation, Texas A&M University, College Station, 2013.

[26] C. K. Madsen, P. Oswald, M. Cappuzzo, E. Chen, L. Gomez, A. Griffin, E. Laskowski, L. Stulz, A. Wong-Foy, "Reset-free integrated polarization controller using phase shifters," *IEEE Journal of Selected Topics in Quantum Electronics,* vol. 11, pp. 431-438, Mar. 2005.

[27] G. E. McGuire, *Semiconductor Materials and Process Technology Handbook for Very Large Scale Integration(VLSI) and Ultra Large Scale Integration(ULSI)*, Noyes Publications, Park Ridge, New Jersey, 1988.

[28] R. V. Schmidt and I. P. Kaminow, "Metal-diffused optical waveguides in $LiNbO_3$," *Applied Physics Letters,* vol. 25, pp. 458-460, Oct. 1974.

[29] K. Sugii, M. Fukuma, and H. Iwasaki, "A study on titanium diffusion into $LiNbO_3$ waveguides by electron probe analysis and X-ray diffraction methods," *Journal of Materials Science,* vol. 13, pp. 523-533, Mar. 1978.

[30] J. L. Jackel, V. Ramaswamy, and S. P. Lyman, "Elimination of out-diffused surface guiding in titanium-diffused $LiNbO_3$," *Applied Physics Letters,* vol. 38, pp. 509-511, Apr. 1981.

[31] Y.-W. Shin, "Electro-optically tunable polarization independent add drop filter with relaxed beam splitter in $LiNbO_3$," Ph.D. Dissertation, Texas A&M University, College Station, 2008.

[32] D. K. Gifford, B. J. Soller, M. S. Wolfe, and M. E. Froggatt, "Optical vector network analyzer for single-scan measurements of loss, group delay, and polarization mode dispersion," *Applied Optics,* vol. 44, pp. 7282-7286, Dec. 2005.

[33] B. L. Heffner, "Deterministic, analytically complete measurement of polarization-dependent transmission through optical devices," *IEEE Photonics Technology Letters,* vol. 4, pp. 451-454, May 1992.

[34] J. Kim, D. B. Adams, and C. K. Madsen, "Device-Under-Test Jones matrix extraction algorithm with device TE/TM reference frame," *IEEE Photonics Technology Letters, IEEE,* vol. 24, pp. 88-90, Jan. 2012.

APPENDIX I

SUBSTRATE CLEANING PROCEDURE

1. Brush and swipe the surface very gently with a Q-tip in soapy water.
2. Rinse several times with D.I. water.
3. Rinse with Acetone.
4. Rinse with Isopropyl alcohol.
5. Rinse with D.I. water.
6. Rinse with Methanol.
7. Blow with N_2 gas

APPENDIX II

PHOTO LITHOGRAPHY PROCEDURE

1. Dehydrate samples in the oven at 135 ^{o}C for 5 minutes.
2. Cool down samples to the room temperature.
3. Spin-coat AZ 5214-IR photoresist at 4500 rpm for 30 seconds on samples.
4. Soft bake samples at 125 °C for 2 minutes.
5. Cool down samples for 10 minutes.
6. Expose samples under UV light with 7 mw/cm^2 power density for 25 seconds without filter.
7. Develop samples in a MF312:H_2O = 1:1.2 solution for 45 seconds.
8. Rinse samples thoroughly with D.I. water.
9. Blow dry samples gently with N_2.

APPENDIX III

REACTIVE ION ETCHING

1. Click ‘stop’ for load pump, and click ‘vent.’
2. Open load dock, and load a sample at the center of the wafer.
3. Click ‘stop’, and click ‘evacuate.’

   (Never click icons for Turbo pump, it will operate automatically.)
4. Input wafer name, and wait until vacuum reaches $8x10^{-6}$ torr. (Roughing will reach $2.8x10^{-3}$ torr, and then turbo pump will automatically operates)
5. Open N_2 valve and process gas valves.
6. Click ‘Process’, and go ‘Recipe’ and input parameters

   i) Ti etch : Forward 100 W, ICP 600 W, Pressure 10 mmTorr,

   Table temperature 20 ^{o}C, CHF_3 30 sccm, Ar 10 sccm, He 10 sccm

   As a preparation step, input the same parameters, except Forward 0W, ICP 0W.
7. After setting up all parameters, click ‘Run’
8. Wait until the process is finished, and click ‘OK’
9. Wait until ventilation in load dock is done, and unload the sample.

APPENDIX IV

DIFFUSION PROCESS

1. Blow a sample with N2, and make sure no dust on a sample surface.
2. Locate a sample at the center of the alumina boat, and insert the boat to the center of the alumina tube.
3. Load the alumina tube in the quartz tube of the furnace, and insert the alumina tube to the center of quartz tube.
4. Cover the furnace entrance with the quartz cap, and connect the outlet of the cap with a water bubbler.
5. Set the temperature parameters for the desired temperature.
6. Open the valve of the breathing air cylinder, and set the flow controller to 100 sccm for 3 bubbles/sec.
7. Flip on the control power switch, wait until all needles point the maximum, and then turn on the element power switch.
8. After desired hours, turn off the element power switch and wait until all needles point the maximum. Then, turn off the control power switch.
9. Wait until the furnace cool down.
10. Unload the sample, and close the air valve and the cylinder.

APPENDIX V

POLISHING PROCESS

1. Place a wet cloth on the clean waveguide surface of a sample to prevent damages from a polishing mount.
2. Place a sample into a polishing mount and secure the mount to a polish jig.
3. Place a diamond disc with a grit size of 15 μm.
4. Turn on the water switch and wait until the disc covered by water.
5. Set the rotation controller to 5 and gently place the polish jig.
6. While holding a polish jig tight, start the rotation controller
7. Inspect the edge of a sample under the microscope and make sure a photoresist rim on the edge of a sample is grinded out.
8. Clean the polished edge with water to prevent damage from the chip of a sample.
9. Turn off water and replace a diamond disc with a grit size of 3 μm.
10. Spread water on the disc and polish a sample with a rotating speed of 4 for 5 min.
11. Inspect the end surface of a sample and repeat until the surface got shiny.
12. Apply a diamond disc with a grit size of 0.5 μm for finer polishing, and polish with a rotation speed of 3.
13. Repeat all procedures for another end of a sample.
14. Clean the surface gently using Q-tip in the soapy water, then wash a sample with water and ethanol.

APPENDIX VI

PHOTO LITHOGRAPHY PROCEDURE ON ALUMINUM FILM

1. Dehydrate samples in the oven at 135 ^{o}C for 5 minutes.
2. Leave samples until they cool down to the room temperature.
3. Spin AZ 5214-IR photoresist at 4500 rpm for 30 seconds on samples.
4. Soft bake samples at 125 °C for 2 minutes.
5. Cool down samples for 10 minutes.
6. Expose samples under UV light with 7 mw/cm^2 power density for 10 seconds without filter.
7. Develop samples in a MF312:H_2O = 1:1.2 solution for 45 seconds.
8. Rinse samples thoroughly with D.I. water.
9. Blow dry samples gently with N_2.